Spatial encoding of forelimb proprioception in the mouse somatosensory cortex

Ignacio Alonso[1], Melanie Palacio-Manzano[1], Irina Scheer[1], Antoine Philippides[2] and Mario Prsa[1]

[1]Department of Neuroscience and Movement Science, University of Fribourg, Switzerland.

[2]Department of Basic Neurosciences, University of Geneva, Switzerland

Abstract

Conscious perception of limb movements depends on proprioceptive neural responses in the somatosensory cortex. In contrast to tactile sensations, proprioceptive cortical coding is barely studied in the mammalian brain and practically non-existent in rodent research. To understand the cortical representation of this important sensory modality we developed a passive forelimb displacement paradigm in behaving mice. We imaged the responses of layer 2/3 neurons with two-photon microscopy and tracked the 3D position of limb joints. In addition, mice were trained to perceptually discriminate proprioceptive stimuli allowing us to delineate the mouse proprioceptive cortex with optogenetic silencing experiments. Our results reveal that passive forelimb movements are preferentially encoded as a spatial direction vector that interfaces movements with behaviorally relevant targets. This neural representation of proprioception appears not to be limited to the somatosensory cortex.

Introduction

Proprioception allows us to detect and track the movements of our limbs. The major target of proprioceptive signals is the cerebellum (spino- and cuneo-cerebellar tracks), involved in maintaining limb posture and adapting movements to unexpected perturbations; processes that typically occur subconsciously (Tuthill and Azim, 2018). Sensory afferents also ascend to the cerebral cortex (dorsal column-medial lemniscus pathway) where proprioceptive information is consciously perceived (Delhaye et al., 2018; Tuthill and Azim, 2018). How the proprioceptive sensation of a limb movement is encoded by neurons in the somatosensory cortex (S1) is still poorly understood. Practically all functional studies of S1 in rodents use extracorporeal (i.e. tactile) stimuli and the few studies in primates on limb proprioception examined cortical responses mainly to active reaching movements (Chowdhury et al., 2020; Goodman et al., 2019; London and Miller, 2013; Prud'homme and Kalaska, 1994). The sensation of an active limb movement is however strongly dominated by motor signals (González-Grandón et al., 2021; Proske and Gandevia, 2012). During muscle contractions, gamma motor neurons tune the sensitivity of both muscle and joint proprioceptors in a manner that is still not fully understood (Dimitriou and Edin, 2008a; Dimitriou and Edin, 2008b). Cortical sensory responses are in addition modulated by motor efference copies during active movements (London and Miller, 2013), which therefore reveal little about how neurons in S1 encode proprioceptive ex-afference on its own. Studying limb movements in the absence of muscle contraction and predictive processing (Keller and Mrsic-Flogel, 2018) is needed to understand the contribution of ascending sensory signals to the cortical proprioceptive code.

In this study, we investigated how passive forelimb movements are represented by the activity of neurons in the mouse S1. Previous similar experiments in primates are few and based on a limited range of stimuli (Chowdhury et al., 2020; Costanzo and Gardner, 1981; London and Miller, 2013; Prud'homme and Kalaska, 1994). We applied highly precise and reliable stimuli using a robotic manipulandum, tracked joint positions with X-ray videography assistance and examined the relationship between movement variables and neuronal responses imaged with two-photon microscopy. We specifically analyzed which aspects of movement (joint kinematics vs. spatial variables) are encoded. Furthermore, we identified additional areas of mouse cortex that are necessary for perceptual proprioceptive discrimination with optogenetic cortical silencing. Our findings provide evidence that limb proprioception in mice is preferentially represented in terms of spatial directions in a non-uniform manner.

Results

Proprioceptive responses in mouse forelimb somatosensory cortex

We trained mice to grasp the endpoint of a robotic manipulandum (Supplementary Fig. 1A) and allow their forelimb to be passively displaced in the horizontal plane. In each trial, the passive movement displaced the limb from the home to the target position and, following a random time delay, back to home (Fig. 1A, Supplementary Movie 1). Mice learned to increase the fraction of correct

trials over successive days of training (Fig. 1B). We simultaneously imaged the Ca^{2+} dependent activity of neurons in the forelimb somatosensory cortex (fS1) with two-photon microscopy (Fig. 1C). The imaged neurons most often responded to the stimuli in a phasic manner (i.e. to the dynamic component of the movement). Occasionally, we also observed sustained responses (tonic or both phasic and tonic) when the forelimb was being held at the target position (Fig. 1D). These three response types are also characteristic of how muscle spindle afferents respond to passive muscle stretch (Cheney and Preston, 1976; Edin and Vallbo, 1990).

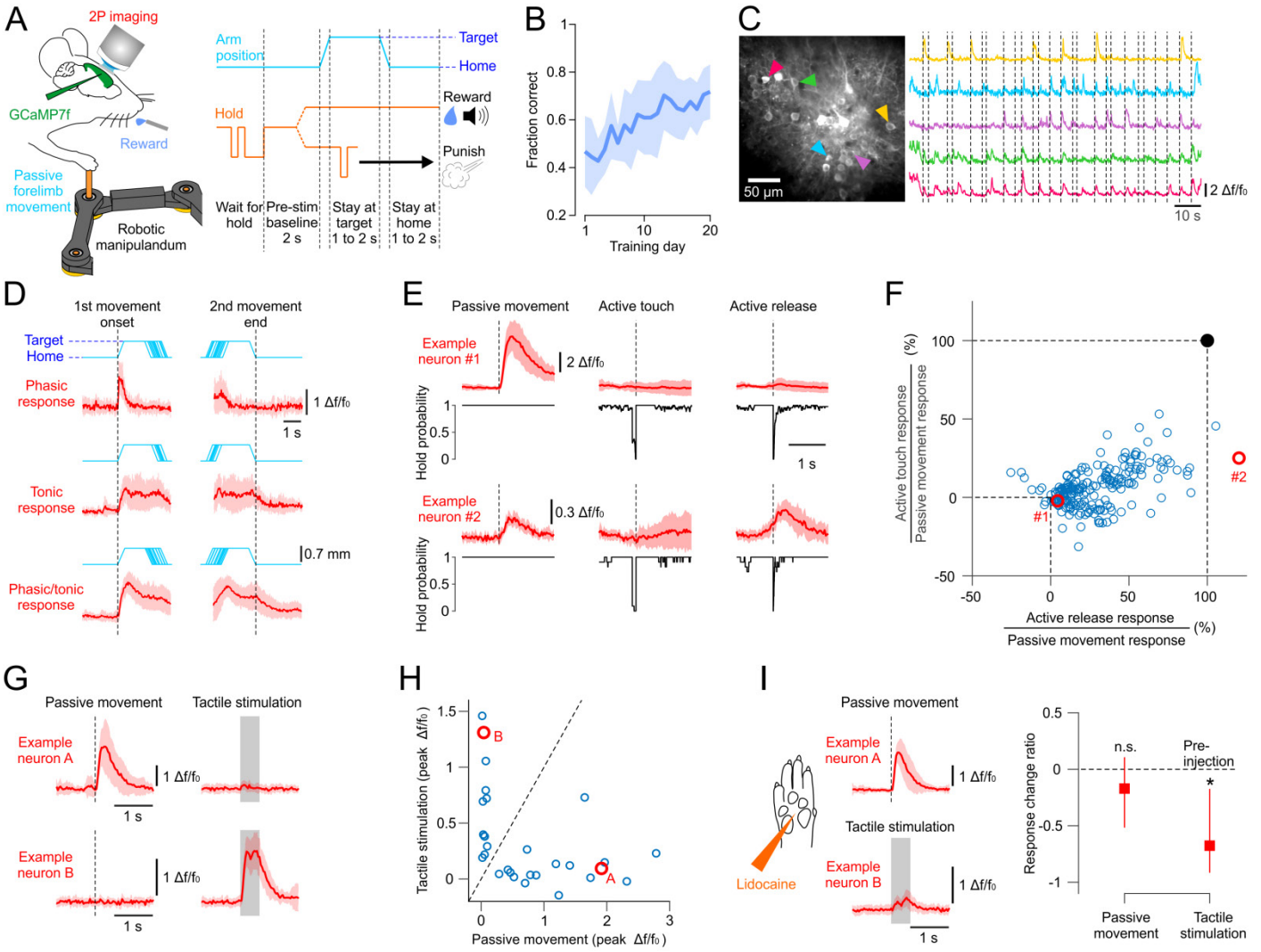

Figure 1. Ca^{2+} imaging of proprioceptive responses in the mouse forelimb S1. A: Experiment schematic and trial timeline of the passive forelimb displacement task. **B**: Average (± s.d.) learning curve (N=13 mice). **C**: Left, cropped two-photon image of the forelimb somatosensory cortex. Right, Ca^{2+} activity traces of 5 neurons (identified in the left panel) responding at the onset of passive forelimb movements (dotted lines, 8 different directions tested). **D**: Three types of observed proprioceptive responses. Ca^{2+} mean (± s.d.) traces of three example neurons (red) aligned to first movement (home-to-target) onset and second movement (target-to-home) end (cyan: individual movement trajectories). **E**: Mean (± s.d.) responses (red) of two example neurons to passive forelimb movement, active touch and active release of the manipulandum. Black traces: instantaneous probability to hold the manipulandum across trials. **F**: Peak responses to active touch and active release as a % of peak responses to passive movement (N=238 neurons, 18 mice). Red circles: data of example neurons in E. **G**: Mean (± s.d.) responses (red) of two example neurons to passive forelimb movement and tactile stimulation of the paw glabrous skin (shaded rectangle indicates the duration of skin indentation). **H**: Peak responses of 29 neurons (2 mice) to passive movement vs. tactile stimulation. Red circles: data of example neurons in G. **I**: Responses after nerve block (s.c. lidocaine injection in the paw) of the two example neurons and the response change ratio of the imaged population (median ± quartiles) relative to their pre-injection levels (N=14 neurons for passive movement, N=12 neurons for tactile stimulation, 2 mice). *: $p<0.01$ n.s.: $p=0.58$ (Wilcoxon signed rank test).

To assess possible contamination by tactile or motor signals, we compared how the neurons respond to active touch and active release events during the pre-stimulus period. Responses to release events were rarely greater, and responses to touch events never greater than those to passive movement (Fig. 1E, F). In addition, we tested

how the neurons respond to passive tactile stimulation of the forepaw (Fig. 1G). There was virtually no overlap between neurons activated by forelimb displacement and those activated by tactile stimulation of the glabrous forepaw skin (Fig. 1G, H). Furthermore, blocking sensory afference from the paw had no significant effect on responses to limb movement, whereas it strongly suppressed tactile responses (Fig. 1I). We conclude that the neuronal responses to passive forelimb movements we imaged in fS1 are proprioceptive in nature.

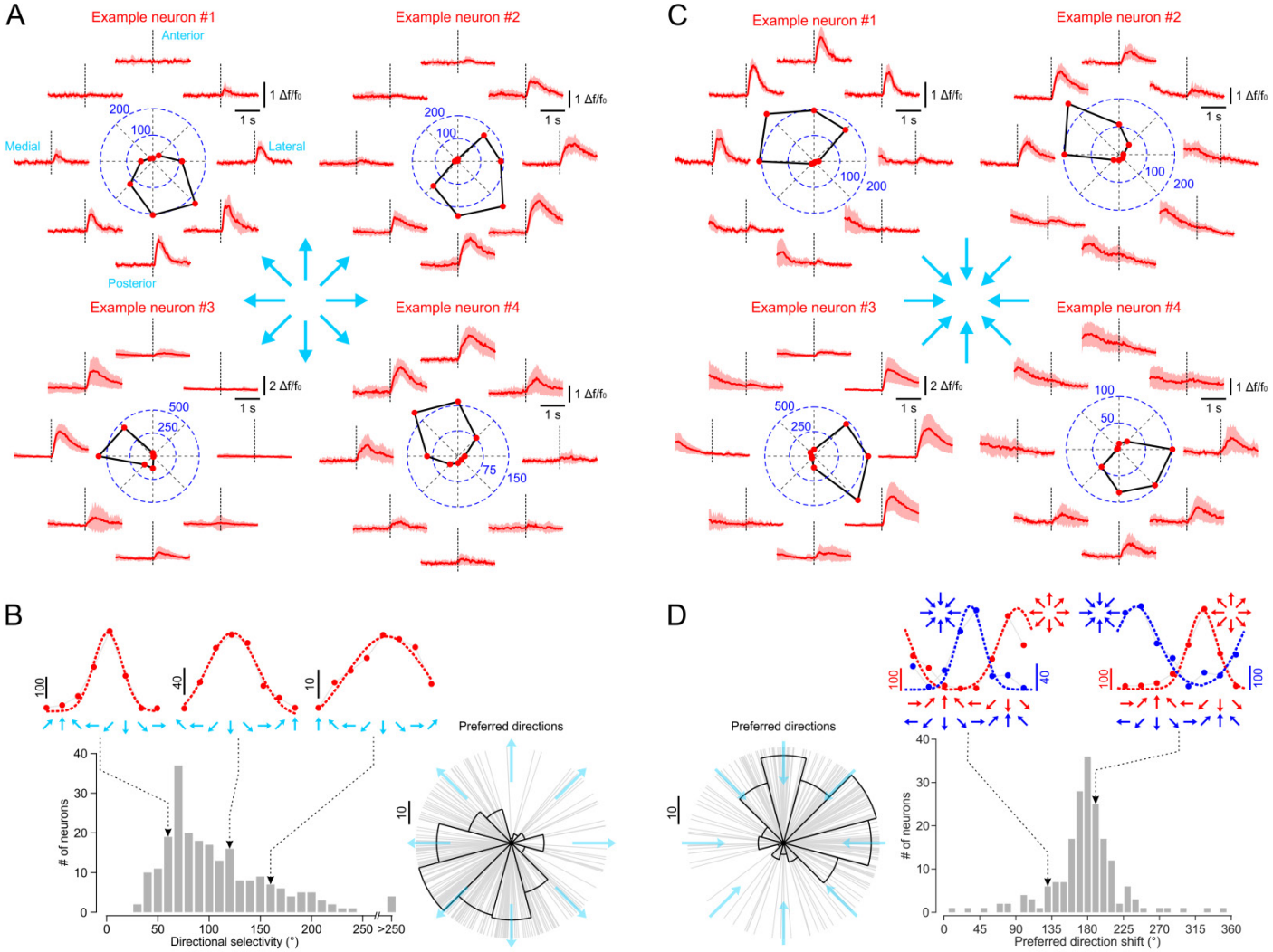

Figure 2. Selective tuning of fS1 neurons to the direction of passive forelimb movement. A: Four example neurons with different preferred directions. Red traces: mean (± s.d.) responses to eight different directions (cyan arrows) of home-to-target movement with the same amplitude (7 mm) and velocity (2 cm/s). Polar plots: peak activity (deconvolved spike rate) as function of movement direction (blue circles and numerical values refer to peak spike rate). Dotted lines: movement onset **B**: Bottom, distribution of directional selectivity and preferred directions (N=226 neurons, 18 mice) for home-to-target movements. Top, Gaussian fits (dotted red lines) to directionally tuned peak responses (deconvolved spike rate) of three example neurons. **C**: same data as in A for target-to-home movements (cyan arrows). **D**: Left, distribution of preferred directions for target-to-home movements (N=197 neurons). Right, distribution of angular shifts in preferred direction between the two movement types (N=187 neurons). Top: Gaussian fits to the directionally tuned responses of two example neurons for home-to-target (red) and target-to-home (blue) movements.

Proprioceptive neurons are directionally selective

In the classic studies in primates, the activity of neurons across motor (Georgopoulos et al., 1982; Mahan and Georgopoulos, 2013) and somatosensory (Prud'homme and Kalaska, 1994) cortical areas was found to be tuned to the spatial direction of active reaching movements. Similar to motor directional tuning, selectivity for directional sensory stimuli is characteristic of neurons in sensory cortices (Bale and Petersen, 2009; Priebe and Ferster, 2005). Data for directional selectivity of somatosensory cortex neurons to passive arm movements in primates is limited and often tested with poorly quantified stimuli (e.g. short arm perturbations or bumps) (Chowdhury et al., 2020; London and Miller, 2013;

Prud'homme and Kalaska, 1994), and is to our knowledge non-existent in rodents.

Here, we imaged fS1 neurons in mice during passive displacements of their forelimbs in eight co-planar directions. The robotic manipulandum produced highly consistent trajectories and movement kinematics in the eight directions (Supplementary Fig. 2), which were therefore unaffected by the impedance of the mouse limb. The activity of almost all responsive cells (>95%) was directionally selective (Fig. 2A, B); their activity could be expressed as a Gaussian function of movement direction (226/238 cells with significant fits). Interestingly, their preferred directions were not uniformly distributed ($p<0.01$, Rayleigh test) across the targeted space. The majority of neurons preferred movements to targets posterior and medial to the home position, and very few to movements in the anterior and lateral directions (Fig. 2B). The non-uniformity is unlikely due to a sampling bias given that the imaged neurons covered the whole antero-posterior extent of fS1 and no obvious directional topography could be observed (Supplementary Figure 3). The opposite preference was observed for movements from targets back to the home position (Fig. 2C, D). Indeed, the angular shift between preferred directions for home-to-target and target-to-home movements was normally distributed around 180° (Fig. 2D). It follows that proprioceptive fS1 neurons are responsive to movement direction per-se rather than driven by the limb crossing a particular spatial location; they are not postural or place cell like representations of a body part in S1 (Long and Zhang, 2021).

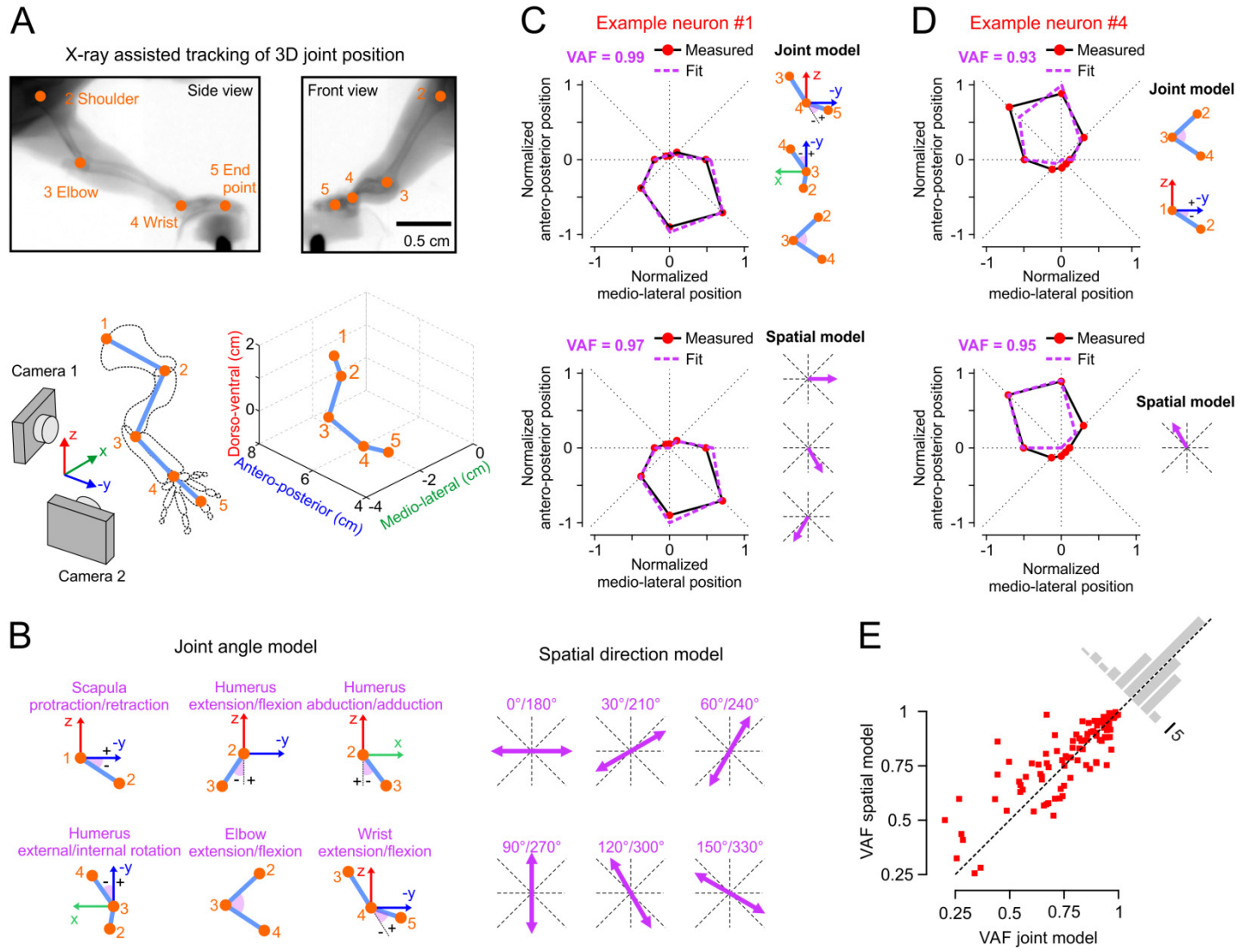

Figure 3. Forelimb joint angles and spatial movement direction can both be encoded by proprioceptive fS1 neurons. A: Identification of mouse forelimb joints with X-ray videography and extraction of their 3D position with stereo cameras. **B**: Definition of joint model and spatial model regressors (6 joint angles and 6 spatial directions, respectively). **C, D**: Joint model and spatial model fits to the directional tuning curves (normalized responses) of example neurons #1 and # 4 (from Figure 2). The included regressors are shown on the right for each fit. VAF: variance accounted for. **E**: comparison of goodness-of-fit (VAF) between the joint and spatial models (N=103 neurons with matched number of regressors).

Proprioception is preferentially encoded in terms of spatial parameters

The non-uniform representation of preferred movement directions (Fig. 2B) seems to suggest that proprioceptive neurons in fS1 are not purely concerned with sensing based on afferent innervation from the limb, but rather with the limb's relation to the body and space. Accordingly, the overrepresented directions might also be those that are more behaviorally relevant since they bring the limb (or held objects) closer to as opposed to away from the body. Alternatively, the non-uniformity might reflect the non-uniform inputs from flexor vs. extensor muscles. Indeed, mice have a much larger extensor: flexor physiological cross-sectional area ratio compared to humans. They also have no brachioradialis muscle; an important forearm flexor in primates (Mathewson et al., 2012). Neurons preferentially driven by lengthening of elbow flexors (i.e. movements in the anterior direction) might therefore be fewer than those driven by lengthening of the extensors (i.e. movements in the posterior direction).

We therefore asked whether proprioception is encoded by fS1 neurons in terms of the limb's end-point spatial displacement (Fuentes and Bastian, 2010; Proske and Gandevia, 2012) or in terms of changes in joint angles / muscle lengths (Chowdhury et al., 2020; Lucas et al., 2019)? Does the tuned activity correlate with the movement directions alone or does it code for specific combinations of joint angles that co-vary with those directions? To answer this question, we first needed to quantify how different limb joints change with movement direction. Joint tracking is however problematic in the mouse forelimb given the absence of clear visual features. The proximal part of the limb is covered by a large volume of skin and subcutaneous adipose tissue which are loosely connected to bones and they do not move in conjunction as a result. The locations of shoulder, elbow and scapulothoracic joints are thus hidden and cannot be identified using standard video tracking methods. To overcome this problem, we placed our setup inside an X-ray fluoroscopy system and acquired images of the limb as it was displaced by the manipulandum throughout the planar workspace (Fig. 3A). The X-ray images guided the identification of joint positions on images of the mouse musculature acquired by a stereo camera system and, after triangulation, allowed extraction of their 3D coordinates (Fig. 3A and Supplementary Movie 2, see Methods for details). We then calculated six joint angles and mapped them onto the planar movement workspace (Fig. 3B and Supplementary Fig. 1). Relative changes in joint angles resulting from any movement within the workspace could thus be read from the obtained joint maps and used as regressors to fit neuronal responses. The joint model was compared to a spatial model comprised of six spatial maps representing the direction of endpoint (i.e. paw) movement (Fig. 3B, Supplementary Fig. 1D-E, see Methods for details).

We used an iterative fitting procedure that only included significant regressors in the full model (see Methods for details). Both models captured the directionally tuned neuronal responses at a generally high and comparable goodness of fit as shown for two example neurons (Fig. 3C-D). When restricting the comparison only to those neurons with an equal number of fitted regressors (i.e. matched model complexity), we observed a marginally significant increase in the goodness of fit for the spatial model (Fig. 3E, $p=0.03$, paired t-test, $N=103$ neurons).

To further identify the preferred proprioceptive neural code, we analyzed to what extent the fitted parameters to home-to-target movements can predict neuronal data during subsequent target-to-home movements. The spatial model predicts that the directional tuning curves are perfectly symmetric in the two conditions because the values of its regressors are independent of starting position for a given movement vector (Supplementary Fig. 1E). The same is not true for joint angles. For example, wrist extension will produce a larger angle for movements in the posterior direction starting from the home position compared to starting from a more anterior position (Supplementary Fig. 1E). Accordingly, example neuron #2 had clearly asymmetric tuning curves for home-to-target vs. target-to-home movements and the data was thus better predicted using the fitted wrist extension regressor (Fig. 4A). Data of example neuron #3 was however better predicted by the spatial model given the more symmetric tuning curves in this case (Fig. 4B). In aggregate, the spatial model could predict the activity better than with just the mean (variance accounted for: VAF>0) in 61% of the neurons (134/221), whereas the joint model only in 51% of the cases (113/223 neurons). Amongst those neurons, the predicted VAF (target-to-home data) compared to the VAF of the fit (home-to-target data) was significantly less reduced for the spatial vs. the joint model (Fig. 4C, $p<0.01$, Wilcoxon rank sum test). The complexity

(fitted number of regressors) between the two models was on average not different (p=0.68, two-sample Kolmogorov-Smirnov test).

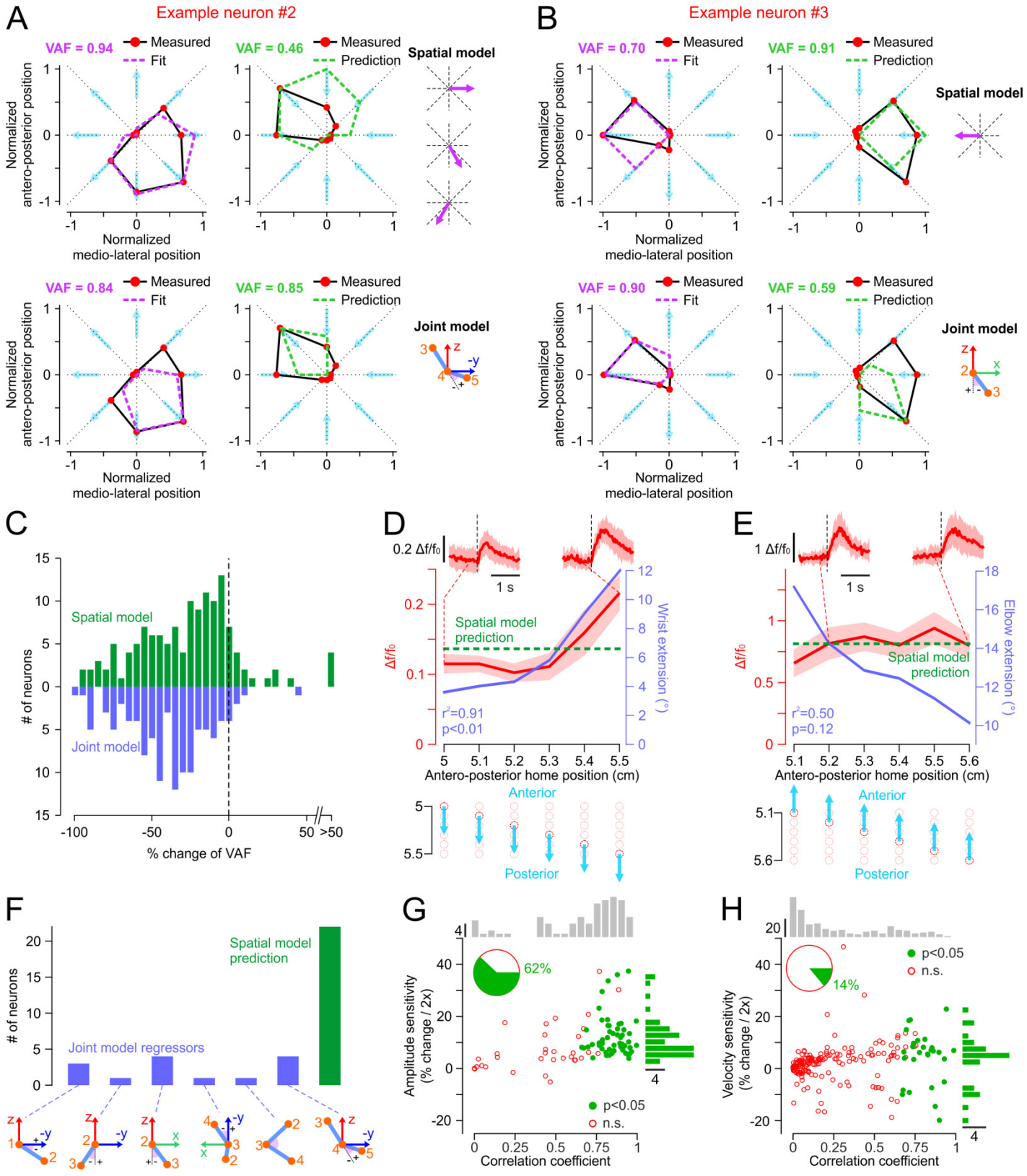

Figure 4. Dominance of spatial vs. joint angle information encoding by fS1 neurons. A: Spatial (top) and joint (bottom) model fits to directional responses of home-to-target movements (left) and their predictions of responses to target-to-home movements (right) for example neuron #2 (form Figure 2). **B**: same data as in A for example neuron #3. **C**: % change in VAF between fits to home-to-target data and predictions of target-to-home data for the spatial (N=134 neurons) and joint angle (N=113 neurons) models. **D**: Mean (± s.d.) peak response (red) of an example neuron for

movements in the posterior direction starting from 6 different home positions (bottom). Blue: absolute change in the wrist extension angle for the same 6 movements. The spatial model (green) predicts identical peak responses for different starting positions. Top, Ca^{2+} average (± s.d.) responses for movements from two different home positions. **E**: Same data as in D for a different example neuron for movements in the anterior direction and compared to absolute change in the elbow extension angle. **F**: Number of neurons whose responses (to movements starting from different home positions) are significantly correlated with changes of different joint angles and of those that are better predicted by the spatial model (i.e. no significant change with home position). **G**: Amplitude sensitivity (% change in peak response for a doubling of movement amplitude) as a function of correlation coefficient (peak response vs. movement amplitude) of neurons tested with varying amplitudes. Top histogram: distribution of correlation coefficients across all neurons. Left histogram: distribution of amplitude sensitivity for neurons with significant correlation with movement amplitude (N=86 neurons, 6 mice). **H**: Data analogous to that in G for neurons tested with varying velocities (N=197 neurons, 8 mice).

To explicitly test the dependence on starting position, in a subset of neurons (N=36, 7 mice) we tested movements in their preferred direction from six different home positions (Fig. 4D-E). We found both neurons with responses correlated to changes in joint angle (Fig. 4D) and those with responses insensitive to starting position as predicted by the spatial model (Fig. 4E). The majority of neurons fell in the latter category (Fig. 4F). There seems therefore to be a clear preference for encoding spatial vs. joint parameters (i.e. the direction in which the endpoint is moving rather than which joints are rotating or muscles lengthening) by fS1 proprioceptive neurons.

It follows that a muscle length (or joint angle) code in primary afferents (Edin and Vallbo, 1990) is elaborated along the ascending pathway into a spatial code in the cortex. To test whether this transformation results in categorically changing neural response sensitivity to movement kinematics, we measured how fS1 neurons are modulated by the amplitude and velocity of the passive movement stimuli in their preferred direction. Whereas primary and secondary muscle spindle afferents are linearly tuned to both the size and rate of change of muscle length (Cheney and Preston, 1976), we observed that fS1 neurons are on average sensitive to amplitude (Fig. 4G) but that only a small minority is significantly modulated by movement velocity (Fig. 4H). Movement size seems to be more spatially relevant than its velocity and might thus explain this categorical difference between peripheral and cortical selectivity to proprioceptive stimuli.

Perception of proprioceptive stimuli depends on the mouse forelimb somatosensory cortex and its adjacent areas

In primates, the cortical recipient of proprioceptive afferents from muscles (also tendons and joints) is Brodmann's area 3a, architectonically distinct from the adjacent somatosensory area 3b receiving cutaneous inputs (Delhaye et al., 2018; Krubitzer et al., 2004). The mouse fS1 has been previously studied in terms of its tactile responses (Gilad and Helmchen, 2020; Prsa et al., 2019) and is thus typically thought of as homologous to area 3b. However, we have here identified neurons in fS1 with prominent proprioceptive responses suggesting a greater degree of functional overlap compared to the primate somatosensory cortex. Indeed, whether the rodent somatosensory cortex has a proprioceptive area (i.e. a homologue of area 3a) distinct from fS1 is unknown (O'Connor et al., 2021). To address this question, we trained VGAT-ChR2 mice to perceptually discriminate between two proprioceptive stimuli (horizontal forelimb adduction vs. abduction) in a two-alternative forced choice task (Supplementary Movie 3) and optogenetically silenced small areas of cortex (Fig. 5A-B, see Methods for details).

Mice could learn the discrimination task at a high level of precision (Fig. 5C); significant discrimination was observed for displacements as small as 0.5 mm ($p<0.05$, binomial test). The stimulus was temporally separated from the answer by a delay period in order to avoid confounds between sensory and motor aspects during inactivation (Guo et al., 2014). Silencing of fS1, but not control sensory or motor areas, significantly decreased the % of correct responses compared to baseline trials without cortical inactivation (Fig. 5D). As inferred from the imaged neuronal responses, we conclude that fS1 is necessary for perceiving not only tactile but also proprioceptive stimuli applied to the forelimb.

Is the mouse proprioceptive cortex limited to fS1 or does it also encompass adjacent areas? Areas such as the transitional zone (TZ) between fS1 and the caudal forelimb motor area (CFA) as well as the dysgranular zone (DZ) between fS1 and the orofacial somatosensory cortex (orfS1) have been hypothesized to be the rodent homologue of area 3a (Chapin and Lin, 1984; Chapin et al., 1987; Cooke et al., 2012; Favorov et al., 2019; Krubitzer et al., 2004). To address this question we inactivated 1 mm strips of cortex centered on these neighboring zones (Fig. 5E). We indeed found that, in addition to fS1, performance significantly decreased also when DZ, TZ or CFA were silenced. As previously suggested (Chapin and

Lin, 1984), we conclude that mouse proprioception has a diffuse cortical representation across several zones that coalesced into a single functional unit (primate area 3a) during the process of evolution.

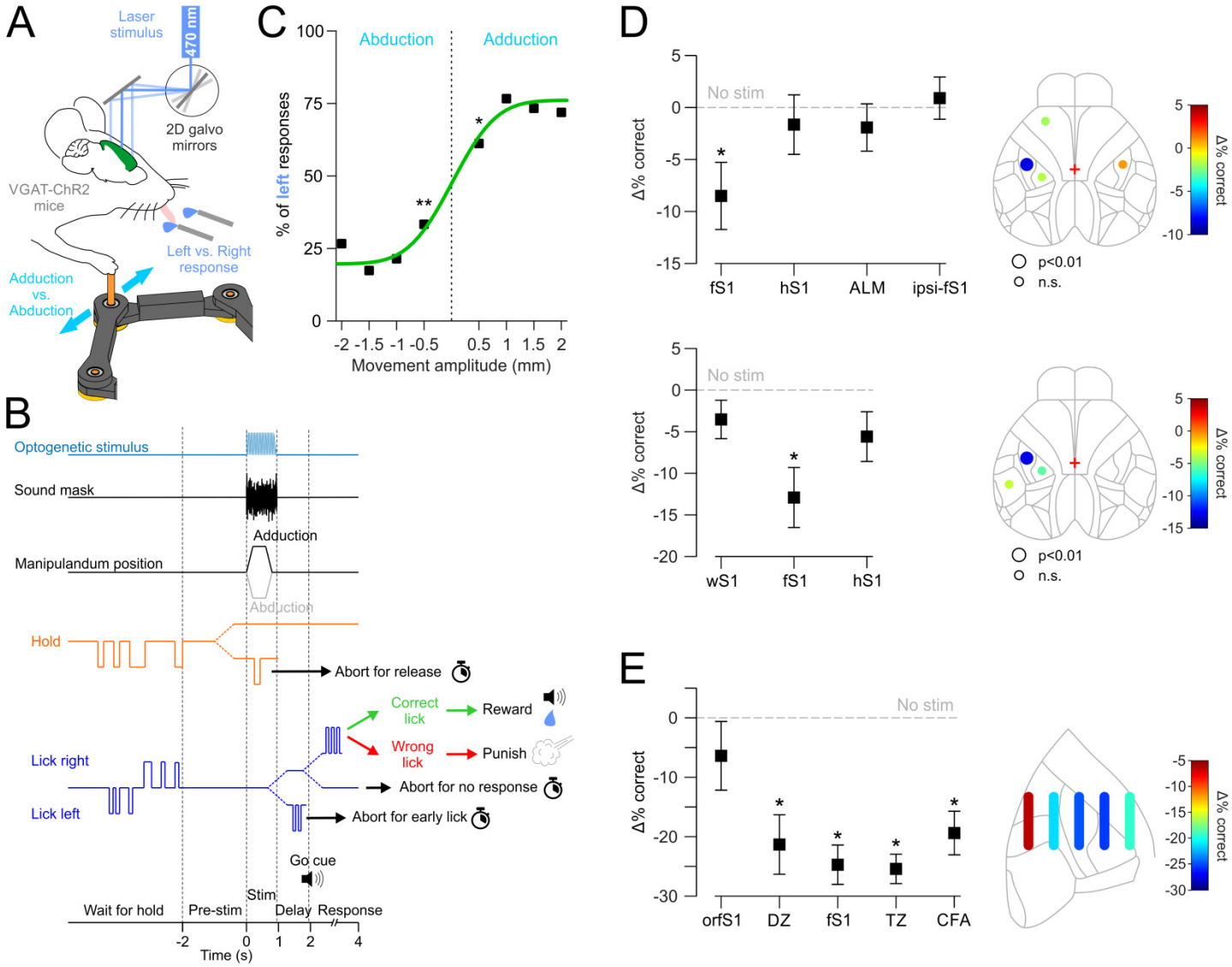

Figure 5. Optogenetic silencing reveals the necessity of fS1 for perceptual discrimination of forelimb proprioception. A: Schematic of the optogenetic silencing experiment during a 2AFC proprioceptive discrimination task. **B**: Trial timeline. **C**: Psychometric discrimination curve of one mouse (N=3 sessions, minimum 45 trials/amplitude). *:p<0.05, **: p<0.01 (compared to 50% chance, binomial test) **D**: Left, decrease in performance (difference in % of correct trials compared to no stimulation, bootstrap mean ± s.e.m.) during selective optogenetic silencing (single point stimulation) of different cortical regions in two mice (top and bottom). fS1: forelimb S1, hS1: hindlimb S1, ALM: anterior lateral motor cortex, ipsi-fS1: ipsilateral fS1, wS1: whisker S1. Right, same data depicted on a schematic of the mouse cortical surface. *: p<0.01 (bootstrap test). **E**: Left, decrease in performance (same statistic as in D) during silencing of cortical regions neighboring fS1 (line stimulation). Right, same data depicted on a zoomed in schematic of the mouse cortical surface. orfS1: orofacial S1, DZ: dysgranular zone, fS1: forelimb S1, TZ: transition zone, CFA: caudal forelimb motor area.

Discussion

Proprioceptive representation of limb movement in mouse somatosensory cortex

A comparison between directional tuning curves for home-to-target and target-to-home movements (Fig. 2) revealed that most imaged neurons encode the direction of movement (a vector code) rather than hand location or limb posture (a position code). The non-uniform distribution of preferred directions showed a striking preference for movements that brought the limb closer to the mouse. We therefore propose that the cortical code specifies whether the limb's endpoint is being displaced away from or towards a behaviorally relevant target (e.g. the body) rather than, for example, whether the elbow joint is being flexed or extended. Spatial direction indeed provided a better account of the neuronal responses than changes in joint angles (Fig. 3E and 4C,F). Our findings thus support the idea that the somatosensory cortex

represents proprioception within a behaviorally relevant spatial context as opposed to as a feedforward sensory map of the body emerging from afferent innervation (Brecht, 2017). This idea is consistent with the observation that the topographic organization of area 3a in primates, and its homologue in other taxa, does not reflect innervation density but emerges and can reorganize as a result of the actual use of the limb in species-specific behaviors (Krubitzer et al., 2004).

How is then a proprioceptive spatial direction signal generated in fS1? Afference from peripheral proprioceptors (e.g. muscle spindles) must be transformed along the ascending pathway to yield a cortical response such as the example neurons in Fig. 4B or Fig. 4E that have "lost" their joint angle specificity. Accordingly, muscle length inputs to a cortical neuron could be continuously tuned by activity representing spatial information in somatosensory cortex (Long and Zhang, 2021; Yin et al., 2018). Spatial activity could be acquired in fS1 based on direct connectivity from limbic structures (Fyhn et al., 2004; Swanson and Köhler, 1986) or cortical areas interconnected with the hippocampal-entorhinal formation (Sauer et al., 2022; Wikenheiser et al., 2021; Wilber et al., 2014). Encoding of space could in fact be a common feature of sensory cortical circuits (Fiser et al., 2016; Town et al., 2017). The observed activity might actually not represent spatial information per se, but instead be a consequence of body simulations proposed to be the key functionality of the somatosensory cortex (Brecht, 2017). The proprioceptive code would thereby specify the movement of a particular body part with respect to another, such as the limb endpoint with respect to the trunk. Regardless, we suggest that the neuronal representation of proprioception in the mouse cortex interfaces limb movements with spatially relevant targets (objects or other body parts) in the physical environment.

The mouse proprioceptive cortex

Both proprioceptive (this study) and tactile (Bandet et al., 2021; Prsa et al., 2019) neurons co-exist in mouse fS1 with seemingly little functional overlap (Fig. 1E-I). Optogenetic silencing of fS1 impairs the perception of proprioceptive stimuli (Fig. 5D) and perceptual discrimination of vibrotactile frequencies also depends on fS1 since it follows the same computation rule as fS1 neuronal activity (Prsa et al., 2019). These findings indicate that, unlike primate areas 3a and 3b, proprioceptive and cutaneous somatosensation do not seem to be segregated in the mouse brain in terms of cortical territory. Our results however suggest that the mouse proprioceptive cortex extends beyond fS1 and comprises the dysgranular zone DZ lying between fS1 and orofacial areas (Chapin and Lin, 1984; Chapin et al., 1987; Sigl-Glöckner et al., 2019), the caudal forelimb motor cortex CFA (Tennant et al., 2011) and a transitional zone TZ (Chapin and Lin, 1984; Cooke et al., 2012) between the latter and fS1 (Fig. 5E). Indeed, responses to joint movements were qualitatively described in the rat fS1, TZ, DZ and CFA analogous areas (Chapin and Lin, 1984). This study also reported that responses were most consistently found in TZ, which was in addition the only area with neurons responding to joint manipulation under anaesthesia. We also found, although not statistically, that the decrease in correct answers was the strongest and most consistently observed when TZ was silenced (Fig. 5E).

Could TZ, the narrow strip between fS1 and CFA nonetheless be the mouse homologue of the primate area 3a? The cytoarchitecture of area 3a is markedly different from area 3b in that it has an attenuated granular layer 4 (L4) and a thick layer 5 (L5). In the mouse cortex, it has recently been documented that the cytoarchitectural transition between fS1 and CFA is gradual (Muñoz-Castañeda et al., 2021); from a cell sparse L5 in fS1 to a denser L5 in CFA and a progressive narrowing of L4 from fS1 to CFA, which is not completely agranular as classically described. Strikingly, a 3D analytical reconstruction revealed individual variations in the architectonic fS1-CFA boundary, which is evocative of the individual variability between animals in the location of area 3a with respect to the central sulcus (Krubitzer et al., 2004). Moreover, TZ in the rat cortex has been suggested to be the homologue of 3a in terms of nociceptive sensing (Favorov et al., 2019). Future experiments using wide field functional imaging of the mouse cortex could more directly compare fS1 to TZ and precisely identify the location of the cortical area most responsive to proprioceptive stimulation.

Implication for neuroprosthetics

To fully replace a paralyzed or lost limb, a neural prosthesis must be bidirectional: as it decodes motor signals, it must simultaneously deliver sensory signals to mimic proprioceptive feedback. One strategy is to stimulate the somatosensory cortex to provide a proprioceptive-like sensation of the prosthetic movement (Dadarlat et al., 2015; Prsa et al., 2017). A crucial question is what kinematic features of the movement should the stimulation paradigm be based on? If our findings in mice

also hold true in primates, they imply that stimulation patterns should be correlated with a movement direction vector of the hand (or its spatial trajectory) rather than with a combination of joint angles.

In agreement with our results, discharge rates of neurons in primate S1 to static arm postures show less variability when plotted against parameters describing spatial hand location than orientation angles in joint space (Tillery et al., 1996). Psychophysical data in humans show that for passive arm displacements, the perception of arm endpoint (Fuentes and Bastian, 2010) and the orientation of the limb relative to gravity (Soechting, 1982) is more precise than the perception of joint angles. Similarly, illusory movements evoked by stimulation of afferents from groups of muscles are not perceived in terms of muscle length or joint angle changes but in terms of the displacement of the limb's endpoint along a given spatial trajectory (Proske and Gandevia, 2012; Thyrion and Roll, 2010). On the contrary, proprioceptive responses of neurons in primate area 2 during reaching movements are better explained by a model based on muscle lengths (Lucas et al., 2019) or whole-arm kinematics (Chowdhury et al., 2020) than by a hand only model. It thus seems that passive proprioceptive afference is preferentially encoded in the cortex and perceived in terms of spatial endpoint kinematics, but that during active behavior the contribution from motor commands (i.e. efference copies) (London and Miller, 2013) and the influence of the fusimotor drive (Dimitriou and Edin, 2008a; Dimitriou and Edin, 2008b) increases the complexity of the cortical code. Indeed, many area 2 neurons stopped representing arm kinematics during passive bumps of the arm (Chowdhury et al., 2020), whereas joint angles were more precisely estimated in active versus passive movements (Fuentes and Bastian, 2010).

We argue nonetheless that a stimulation paradigm based on the neural representation of passive proprioception is better suited for neuroprosthetic movement restoration. If the aim is to evoke a proprioceptive-like percept, then sensory ex-afference is perceptually more salient than sensory re-afference resulting from active movements (Proske and Gandevia, 2012). Muscles in paralyzed or non-existent limbs do not contract and decoded motor activity bypasses a large part of the descending motor circuitry. Therefore, engaging the perceptual instead of the motor proprioceptive pathway (Chowdhury et al., 2020) seems to be more relevant for neuroprosthetic control.

Materials and Methods

Mice

For Ca^{2+} imaging of cortical neurons we used 16 C57BL/6 mice (Charles River Laboratory) and 3 Thy1-GCaMP6f-GP5.17 mice (Jackson laboratory; stock no. 025393). For optogenetic silencing experiments we used 2 VGAT-ChR2-eYFP mice (Jackson laboratory; stock no. 014548). All mice were male and 8 to 12 weeks old at the start of experiments. Mice were housed in an animal facility in groups of maximum five per cage, maintained on a 12h/12h light/dark cycle and placed on a water restriction regime of 1 ml/day during experiments. All procedures were approved by and complied with the guidelines of the Fribourg Cantonal Commission for Animal Experimentation.

Surgical procedures for two-photon imaging experiments

Surgeries were performed under isoflurane anesthesia (1.5 to 2% in 1.5 L/min O_2). We administered additional analgesic (0.1 mg/kg buprenorphine intramuscular (i.m.)), local anaesthetic (75 µl 1% lidocaine subcutaneous (s.c.) under the scalp) and anti-inflammatory drugs (2.5 mg/kg dexamethasone i.m. and 5 mg/kg carprofen s.c.). Mice were fixed in a stereotaxic frame and rested on a heating pad (37°C). An incision was made over the midline between the ears and eyes to expose the scalp. To allow for head fixation during experiments, a titanium head frame was fixed on the skull with a cyanoacrylate adhesive (ergo 5011, IBZ industrie) and clear dental acrylic (Paladur, Kulzer GmbH). We made a craniotomy centered over the left forelimb somatosensory cortex (fS1) and performed five viral injections at stereotaxic coordinates -2.25 mm lateral and from -0.25 mm to 0.75 mm in 0.25 mm steps anterior to bregma (based on localization of fS1 in mice with intrinsic signal imaging (Prsa et al., 2019)) using pulled and beveled (≈25 µm tip diameter) glass pipettes (Wiretroll II, Drummond Scientific). We injected AAV9/2-hSyn1-jGCaMP7f (Zurich Viral Vector Facility, v292-9, stock titer $4.4x10^{12}$ vg/ml) in 12 C57BL/6 mice and AAV9/2-hSyn1-jGCaMP8m (Zurich Viral Vector Facility, v623-9, stock titer $6.4x10^{12}$ vg/ml) in 4 C57BL/6 mice (1:10 dilution with 0.2% FastGreen in sterile saline) at a depth of 350 µm, 30 to 60 nl per site at a rate of 20 nl/min. After rinsing the cortical surface with dextamethasone (0.01 ml of a 4 mg/ml solution) we covered the craniotomy with a cranial window. The window consisted of two hand-cut glass coverslips (150

µm) glued together with optical adhesive (NOA 61, Norland). The lower one, matching the shape of the craniotomy, was placed on the cortical surface and the top one, cut to 1 mm larger than the craniotomy, was fixed to the skull with cyanoacrylate glue and dental acrylic. Experiments typically began 14 days after surgery. The same surgery but without viral injections was performed in the Thy1-GCaMP6f-GP5.17 mice.

Surgical procedures for cortical silencing experiments

Under the same anesthesia protocol, VGAT-ChR2-eYFP mice were implanted with a titanium head frame as above. We made a transparent skull preparation for transcranial optical access (Guo et al., 2014; Morandell and Huber, 2017; Xu et al., 2022). All periosteum was removed from the skull surface and the area thoroughly cleaned. The skull surface was homogenously covered with a thin layer of transparent dental acrylic (Paladur, Kulzer GmbH). After curing, a drop of cyanoacrylate adhesive (ergo 5011, IBZ industrie) was spread on the coated surface and made the skull transparent.

Robotic manipulandum

We custom-built a robotic manipulandum based on the planar 2 DOF pantograph design (Campion et al., 2005; Vigaru et al., 2013; Wagner et al., 2020). The robot consists of four CNC machined aluminum arm linkages connected to each other at three joints (Supplementary Fig. 1A) using miniature ball bearings (Reely MR 52 ZZ, 2 mm Ø). A handle (steel rod, 2 mm Ø, with the tip rounded for comfortable grasping) is mounted at the endpoint joint. The mechanism is mounted on and actuated by two DC motors (DCX22L EB SL 9V, Maxon Motors) with integrated optical rotary encoders (ENX 16 RIO, 32768 counts/turn, Maxon Motors). A 1:16 reduction gear (GPX22 A, Maxon Motors) is mounted on each unit to maximize position stability during actuation (i.e. uniformly counteract the impedance of the mouse limb, Supplementary Fig. 2) and increase angular positioning resolution. The motors are operated in position mode with the EPOS2 24/5 positioning PID controllers (Maxon, 1 kHz sample rate) and interfaced via USB with Matlab using EPOS2 libraries. Transformations between angular coordinates of the motors and planar Cartesian coordinates of the manipulandum's endpoint are coded in Matlab by computing the forward and inverse kinematics of the linkage structure (Campion et al., 2005). The angular position of each motor was read via USB and used to compute and monitor online the instantaneous position of the manipulandum at a rate of 100 Hz. In parallel, we recorded the position at a 1 kHz sampling rate with a custom-built circuit. The quadrature signals from the optical encoders were decoded using the hardware quad decoders of Arduino DUE and the 16-bit digital signals at its output transformed to analog signals (AD669ANZ, Analog devices). The analog signals were sampled at 1 kHz (NI PCIe-6321, National Instruments) and logged to disk.

Behavioral procedures

All behavior was controlled and measured with real-time protocols using the Bpod State Machine r1 system (Sanworks) interfaced with Matlab. We created a Matlab object as a plugin to the Bpod code in order to control the robotic manipulandum from within a Bpod protocol.

Passive forelimb movement task

Mice sat head fixed inside a tube and trained to hold the robotic manipulandum handle with their right paw. The home position (i.e. the forelimb endpoint) was located approximately 17 mm below, 2.5 mm lateral and 10 mm posterior to the mouse snout. Contact with the handle was detected with a capacitive sensor (MPR121, Adafruit interfaced with an Arduino Nano Every board). Each trial began with a pre-stimulus baseline requiring 2 s of continuous holding. A release resulted in resetting the 2 s wait period. The manipulandum was then displaced radially from its home position to a target position in one of 8 co-planar cardinal directions with a trapezoidal velocity profile (3 cm/s). The movement amplitude was between 5 and 8 mm. After a random 1 to 2 s holding period at target position, the manipulandum returned to its home position followed by a second 1 to 2 s random holding period (Supplementary Movie 1). Releasing the handle at any time during the trial resulted in a punishment (air puff to the face) and an aborted trial. Continuous holding resulted in a correct trial and a water droplet reward (Fig. 1A). In the amplitude and velocity tests (Fig. 4G, H), between 1 and 4 directions were tested simultaneously. Seven different amplitudes between 2 mm and 8 mm (at a fixed velocity) and six different velocities between 2 and 4 cm/s (at a fixed amplitude) were tested.

Perceptual discrimination task

Mice had to perceptually discriminate between two directions of passive forelimb movement with a directional lick toward one of two reward spouts (Supplementary Movie 3). Each trial started with a 2 s pre-stimulus period (as above) requiring continuous holding and no licking of the reward spouts. During the subsequent stimulus period, the manipulandum passively displaced the right mouse forelimb either laterally (i.e. abduction) or medially (i.e. adduction),

stayed at the target position for 400 ms and returned home. An auditory mask (white noise sampled at 50 kHz to cover the hearing range of the mouse) was played on a loud speaker during the stimulus to mask the sound of the motors. We tested displacement sizes between 0.5 and 4 mm at a 2 cm/s velocity. The optogenetic silencing results are based on 4 mm displacements (Fig. 5). The stimulus was followed by a delay period, an auditory go cue and an answer period (Fig. 5B). During the answer period (limited to 2 s), if the mouse licked the correct water spout (right for abduction and left for adduction) he received a water droplet at that spout or an air puff for the incorrect licking direction. The opposite stimulus/answer rule (i.e. reversed contingency) was used for the second mouse. Releasing the handle during stimulation, licking during the stimulus or delay periods and not answering resulted in an aborted trial and a 4 s timeout. Holding and licking was detected with a capacitive sensor (MPR121, Adafruit). To minimize a directional licking bias, the probability of an abduction trial (P_{abd}) was determined in real-time as a function of the measured bias during the last 10 non-aborted trials. The bias value was calculated as the difference in the fraction of correct responses between abduction and adduction trials. P_{abd} was calculated at the start of each trial according to the double sigmoidal function:

$$P_{abd} = 1 - \frac{0.5}{1 + \left(\frac{bias + 1}{\tau_1}\right)^{S_1}} - \frac{0.5}{1 + \left(\frac{bias + 1}{\tau_2}\right)^{S_2}}$$

Where the inflection slopes S_1 and S_2 at the chosen inflection points τ_1=-0.5 and τ_2=0.5 were set to 30 and 12 respectively.

In the first 5 to 7 days of training, the reward was automatically delivered at the correct spout during the go-cue while maintaining all trial abort rules. This allowed mice to first learn the abort rules as well as the stimulus/response association.

Tactile stimulation

Tactile stimuli (Fig. 1G-I) were automatized indentation of the paw's glabrous skin using a custom-built device. A nylon bristle (0.35 mm diameter) was mounted on a push-pull solenoid (Adafruit 412) actuated by relaying a 12 V signal from a high current source (custom circuit) with a TTL pulse from Bpod. Foam material was added to the solenoid base to limit its full travel and thereby mask sound. The displaced bristle traveled through the center of a paw holder (3D printed) and evoked a ≈1 mm skin indentation lasting 500 ms. Successive stimuli occurred randomly, only when the mouse had its paw placed on the holder and were separated by at least 3 s.

Nerve block

Mice were briefly anaesthetized with isoflurane (3%). Neural transmission from the forepaw was blocked with a single 10 µL injection of lidocaine (1%) in the palm (s.c.). Mice were subsequently head-fixed under the two-photon microscope and allowed to recover from anaesthesia for ≈10 min before starting the experiment. The imaged responses were compared to those of the same neurons obtained pre-injection (Fig. 1I).

Two-photon microscopy

Ca^{2+} imaging in the mouse cortex was performed with a custom built two-photon microscope based on an open source design (MIMMS 2.0, janelia.org/open-science) and controlled with Scanimage 5.7_R1 software (Vidrio Technologies) and National Instrument electronics. The Ti:Sapphire excitation laser (Tiberius, Thorlabs) was tuned to 930 nm and focused with a 16x 0.8 NA objective (Nikon) below the cortical surface. The laser power (typically 25 mW measured at the objective) was modulated with pockels cell (350-80-LA-02, Conoptics) and calibrated with a Ge photodetector (DET50B2, Thorlabs). A 550 µm by 550 µm area of cortex was scanned at ≈30 frames/s using a resonant-galvo scanning system (CRS8K/6215H, CRS/671-HP Cambridge Technologies). Emitted fluorescence was detected with GaAsP photomultiplier tubes (PMT2101, Thorlabs) and the acquired 512 x 512 pixel images written in 16 bit format to disk. Behavioral event (trial start and stimulus onset) TTL pulses issued by the Bpod State Machine were received as auxiliary inputs to the Scanimage electronics and their timestamps saved in the headers of the acquired images. The timestamps were used to temporally align neuronal data to behavioral events.

Optogenetic silencing

Cortical silencing was achieved by optogenetic activation of GABAergic cortical neurons (i.e. indirect inhibition of excitatory neurons) in VGAT-ChR2-eYFP mice through the clear skull preparation using a 473 nm laser (Obis LX FP 473, Coherent) operated in analog control mode. This silencing method is shown to be more effective that direct inactivation of excitatory cells using inhibitory opsins (Li et al., 2019). The optical fiber from the laser was inserted into an aspheric

collimator (CFC11A-A, Thorlabs) and the resulting free space beam aimed at cortical coordinates with a pair of galvanometric scanning mirrors (PT-A40, Phenix Technology). The laser beam was focused on the cortical surface with an achromatic doublet lens (AC254-100-A, Thorlabs) and gated with a shutter (SHB05T, Thorlabs). The laser power and position of scanning mirrors were controlled by analog signals from the Bpod analog output module (Sanworks). The laser power modulation signal was a 40 Hz sinusoid of duration equal to the stimulation period. The last 100 ms of the signal were ramped down linearly. The mean power of the stimulation signal used in our experiments was 1.5 mW (measured at the cortical surface). Scanner controller voltages corresponding to the coordinates of the silenced regions (Fig. 5D,E) relative to bregma (fS1: -2.25 mm lateral, 0.25 mm anterior; hS1: -1.75 mm, -0.75 mm; ALM: -2 mm, 2 mm; ipsi-fS1: 2.25, mm, 0.25 mm; wS1: -3.5 mm, -1.5 mm; orfS1: -3.5 mm, 0.25 mm; DZ: -3 mm, 0.25 mm; TZ: -1.75 mm, 250 mm; CFA: -1.4 mm, 250 mm) were calculated using a calibration head frame and the reference (0,0) coordinate was aligned to bregma at the start of each session. The line stimuli (Fig. 5E) were 1 mm long, centered on the respective area's coordinate and produced by a 40 Hz triangular wave oscillation of the scanning mirror. Three targets were inactivated per session on 1/3 of the trials. On the remaining 2/3 the laser was aimed at a control site outside of the cortical surface (posterior end of the head frame). The inactivation trials were therefore not visually cued as the blue light stimulus was present on every trial.

X-ray assisted 3D joint tracking

The corpse of an adult mouse (≈25 g) was head fixed and its right forelimb stuck to the manipulandum endpoint using the same apparatus configuration as in the experimental condition. The apparatus was placed in a C arm fluoroscope (Philips BV 25) and the forelimb displaced in succession to each point of the planar workspace (as defined in Supplementary Fig. 1B). The acquisition (Matrox Solios eCL-B frame grabber) of the detected x-ray images (Dexela 1207 flat panel ray detector) were triggered by TTL pulses (NI PCIe-6321, National Instruments) from the PC controlling the manipulandum's position (see above). The acquisition was repeated at two orientations relative to the source/detector axis (side and front views in Fig. 3A). Independently, we acquired video images at the same manipulandum positions after surgically removing the skin and adipose tissue of the mouse's forelimb by two cameras simultaneously (Basler dart USB 3.0, daA1280-54um, 1280 x 960 resolution with a 8 mm Evetar IR lens). The two cameras were pointed at the skinned forelimb from two different orientations in the horizontal plane and externally triggered by the same TTL pulses. A side-by-side comparison of the X-ray and video images allowed us to precisely hand score the locations of the endpoint and 4 joints (scapulothoracic, glenohumeral, elbow and wrist) on the limb musculature of each stereo image pair using a custom graphic user interface programmed in Matlab. Using a checkerboard pattern and the Matlab *Stereo Camera Calibrator App* we obtained the stereo calibration parameters of our stereo camera configuration. We subsequently calculated the world 3D positions of each joint (with the optical center of camera 1 as the origin) using the *triangulate* function in Matlab by passing the stereo camera coordinates and calibration parameters as inputs. To transform the 3D positions from camera into manipulandum coordinates (where the origin is the center of the left motor as shown in Supplementary Fig. 1A-B), we first fit a geometric transformation based on rotation, scaling and translation (without reflection and shearing) between the manipulandum positions (in manipulandum coordinates) and the tracked positions of the endpoint (in camera coordinates) using the *fitgeotrans* Matlab function. The fitted transformation was then used to transform the camera into manipulandum coordinates with the *transformPointsForward* function. Prior to the transformation, the values were converted from mm to cm, the Y and Z axes swapped and the Z axis inverted.

We calculated 6 joint angles (scapula protraction/retraction, humerus extension/flexion, humerus abduction/adduction, humerus external/internal rotation, elbow extension/flexion, wrist extension/flexion) from the 3D joint coordinates (Supplementary Movie 2) for each position on the planar workspace (Supplementary Fig. 1D). The calculation of each joint angle is graphically defined in Fig. 3A-B: scapula protraction/retraction is the azimuth angle between the -Y axis vector and the vector of the scapula (link defined by points 1 and 2) projected on the YZ plane, humerus extension/flexion is the azimuth angle between the -Z axis vector and the vector of the humerus (link defined by points 2 and 3) projected on the YZ plane, humerus abduction/adduction is the azimuth angle between the -Z axis vector and the vector of the humerus (link defined by points 2 and 3) projected on the XZ plane, humerus external/internal rotation is the azimuth angle between the -Y axis vector and the vector of the ulna/radius (link defined by points 3 and 4) projected on the XY plane. Wrist extension/flexion is the difference between two angles: the azimuth angle between the Y axis vector and the vector of the ulna/radius (link defined by points 4 and 3) and the azimuth angle between the -Y axis vector and the vector of the autopod (link defined by points 4 and 5) both projected on the YZ plane. Elbow extension/flexion is calculated as $atan2(\|S_1 \times S_2\|, S_1 \cdot S_2)$ where $S_1 = P_2 - P_3$, $S_2 = P_4 - P_3$ and P_2, P_3 and P_4 are the

3D coordinates of the shoulder, elbow and wrist joints (points 2, 3 and 4) respectively. Two additional joint angles (humerus external/internal rotation and wrist ulnar/radial deviation) were computed but excluded from analysis due to negligible changes during tested movements. Wrist pronation/supination was not tracked and judged to be negligible for translational limb movements.

Two-photon data processing

Motion correction

A custom MATLAB registration script was used to correct for vertical and horizontal image movements. Each acquired image was aligned to a baseline average image recorded at the start of each session. We computed the cross-correlation between each image and the template by multiplying the two-dimensional discrete Fourier transform of one with the complex conjugate of the Fourier transform of the other and taking the inverse Fourier transform of the product. The X and Y location of the peak cross-correlation value gave the vertical and horizontal shift, respectively. 10% of each image was cropped at the boundaries before carrying out the computation.

Region of interest and Ca^{2+} activity generation

Using the session mean and variance images, soma centers of active neurons with clearly identifiable morphologies were manually initialized. Regions of interest of individual neurons and background were then identified as spatial footprints using the constrained nonnegative matrix factorization method (Giovannucci et al., 2019) from the CaImAn Matlab toolbox (github.com/flatironinstitute/CaImAn-MATLAB). The time-varying calcium activity of each neuron (i.e. its spatial footprint) and their time-varying baseline fluorescence was subsequently extracted from the acquired images and used to compute $\Delta f/f_0$ traces used for analysis.

Spike rate deconvolution

Spike rate was inferred from the $\Delta f/f_0$ traces using the OASIS deconvolution algorithm (Friedrich et al., 2017) of the Suite 2P toolbox (github.com/cortex-lab/Suite2P) with a 0.8 s sensor timescale. Spike rate density was calculated by convolution of the inferred spikes with a Gaussian kernel (0.1 s width, 1 kHz sampling rate) and multiplying the result with the sampling rate.

Data analysis

Stimulus evoked responses

The stimulus evoked $\Delta f/f_0$ (or inferred spike rate) response was defined as the difference between the maximum post stimulus value (in the 0 to 1.5 s interval relative to onset) and the mean value pre-stimulus value (between 0 s and -0.75 s relative to onset). Significant responses were identified with a randomization test at significance level $p<0.01$. Specifically, the response calculation for each neuron was repeated 1999 times for randomly shifted stimulus onset times across the neuron's activity trace of the session. The 1999 calculated chance measures were compared to the non-randomized response and the latter was deemed significant if it was more extreme than the upper 99th percentile of the chance values distribution.

Directional selectivity

Directional selectivity was tested by fitting a Gaussian function $f(x) = b_0 \exp(-\left(\frac{x-b_1}{b_2}\right)^2)$ to the neuron's stimulus-evoked responses (inferred spike rate) in the 8 tested directions. The directional responses were first shifted circularly to center the data on the direction with the maximum response. A neuron was deemed to be directionally selective if the 95% confidence intervals of the b_0 and b_2 fitted parameters did not include zero. The neuron's preferred direction and directional selectivity were defined by the b_1 and b_2 fitted parameters, respectively.

Joint and spatial model fits

Neuronal responses to movements in the eight tested coplanar directions were fit using an iterative procedure. Six joint angle and six spatial direction maps (Supplementary Fig. 1D, E) were used as linear regressors to fit the data. The joint angle maps were calculated as described above (see 3D joint tracking). The values of the six spatial direction maps were calculated for each medio-lateral $X_{i,j}$ and antero-posterior $Y_{i,j}$ coordinate of the planar workspace (red grid in Supplementary Fig. 1B) as:

$$S_{i,j}^{\tau} = [\cos\tau \sin\tau] \times \begin{bmatrix} X_{i,j} \\ Y_{i,j} \end{bmatrix}$$

for τ = 0°, 30°, 60°, 90°, 120° and 150°. These spatial maps were chosen to conveniently match the number and nature of the joint angle maps. We do not hypothesize that a neuronal representation of these spatial maps exists. Rather, it is a convenient way to represent information about the spatial direction of movement and compare it to the joint angle representation.

For each movement direction, the regressor value was the change in joint angle or spatial direction data between the home and target position. For each model, we first fit the neuronal responses with each regressor independently. The regressors were then ordered in terms of their goodness of fit (the noise variance) and the initial model included only the first regressor in the list (the one yielding the lowest noise variance is assumed to be included in the full model). We then iteratively added the other regressors one by one to the model and only kept them if their addition yielded a significant improvement in the goodness of fit (F-test, $p<0.05$). The F-test statistic was calculated as the difference between the sum of squared errors of the initial and updated models, divided by the noise variance of the updated model. The goodness of fit (Fig. 3C-E) and prediction (Fig. 4A-C) was evaluated with the variance accounted for (VAF) measure as $1 - var(F_{est} - F_m)/var(F_m)$ where F_{est} is the estimated (fitted or predicted) and F_m the measured neuronal activity. The comparison between the joint angle and spatial direction model fits (Fig. 3E) only included neurons for which the two models had a matched number of regressors.

Linear regression fits to the neuronal responses to movements starting from different home positions was performed for single joint angle regressors (Fig. 4D-F). The spatial model prediction (i.e. no change in neuronal response for different home positions) was deemed to better account for the data if none of the joint angle regressors nor a line model (slope and offset model) yielded a significant fit.

Behavioral data analysis

In the perceptual discrimination task, the Δ% correct (Fig. 5D,E) for each inactivation site was defined as the drop in % of correct responses compared to the control site. Data from 8 to 10 sessions were pooled for each mouse and inactivation site. A bootstrap test of the Δ% correct statistic being different from zero was performed by taking at random, with replacement, N values from the total set of N measurements, 1999 times. The one-tailed bootstrap p value was computed as the ratio of 1999 Δ% correct sample measurements more extreme than zero. The bootstrap standard error of the mean was calculated as the standard deviation of the 1999 Δ% correct sample measurements.

Psychometric curve fitting

In the perceptual discrimination task, we analyzed the fraction of left lick responses as a function of directional displacement amplitude (Fig. 5C). The data was fit with a sigmoid function (i.e. a cumulative Gaussian, including the lapse rate and guess rate parameters) using the psignfit Matlab toolbox (Schütt et al., 2016). Data from 3 sessions were pooled together yielding at least 45 trials per tested amplitude.

Supplementary material

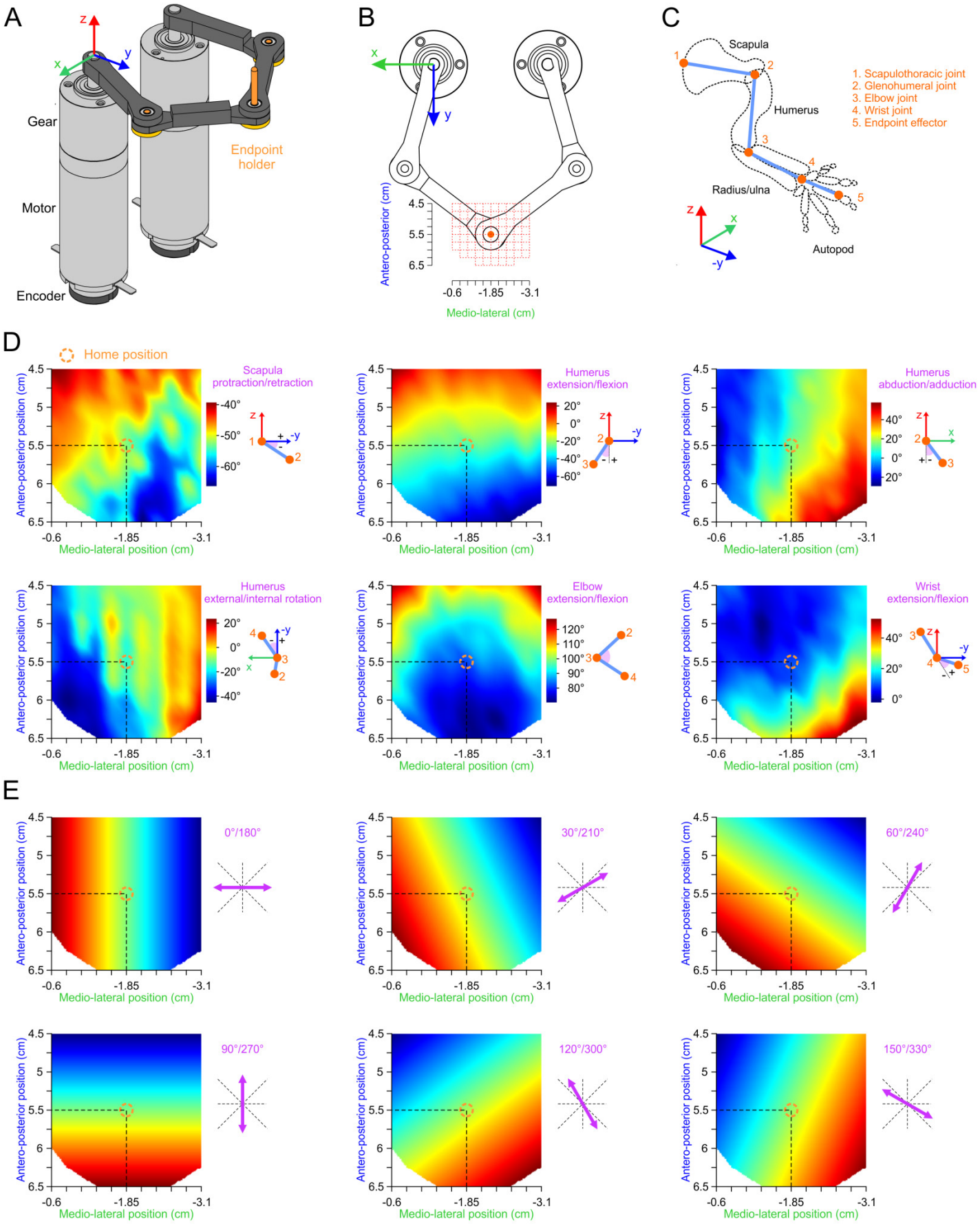

Supplementary Figure 1. Joint angles and endpoint spatial directions mapped onto the planar workspace of the robotic manipulandum A: CAD model of the robotic manipulandum showing the origin of the Cartesian coordinates. **B**: Top view of the manipulandum showing the workspace of

forelimb movements (red grid). **C**: Definition of tracked joints. **D**: Tracked joint angles (color map, linear interpolation) mapped onto the planar workspace. Each angle was measured at every point of the workspace defined in B (red grid). **E**: Definition of endpoint spatial directions mapped onto the same workspace.

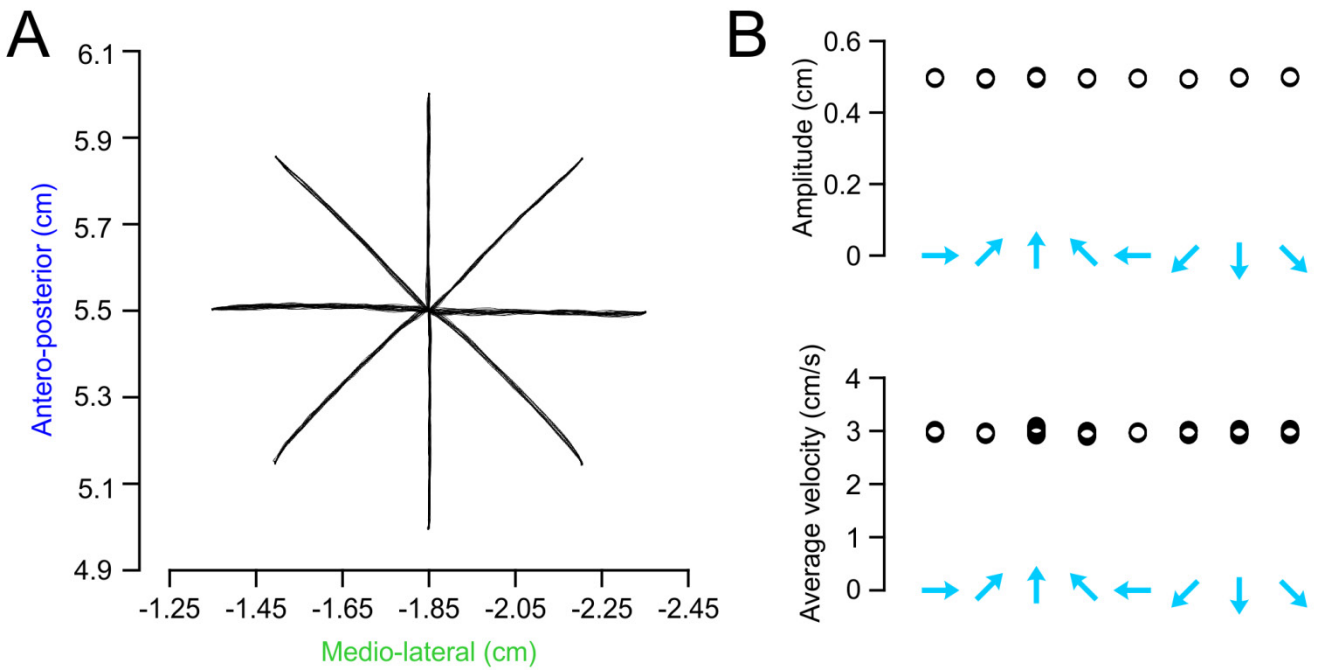

Supplementary Figure 2. Consistent movement kinematics. A: Superimposed 2D trajectories of the manipulandum's endpoint (raw unfiltered measurements with the optical encoders and sampled at 1 kHz, see Methods) for movements in the eight tested directions in an example session (17 to 23 trials per direction, 0.5 cm amplitude and 3 cm /s velocity). **B**: Measured 2D amplitudes and average velocities of the individual movements in A were highly consistent across the tested directions.

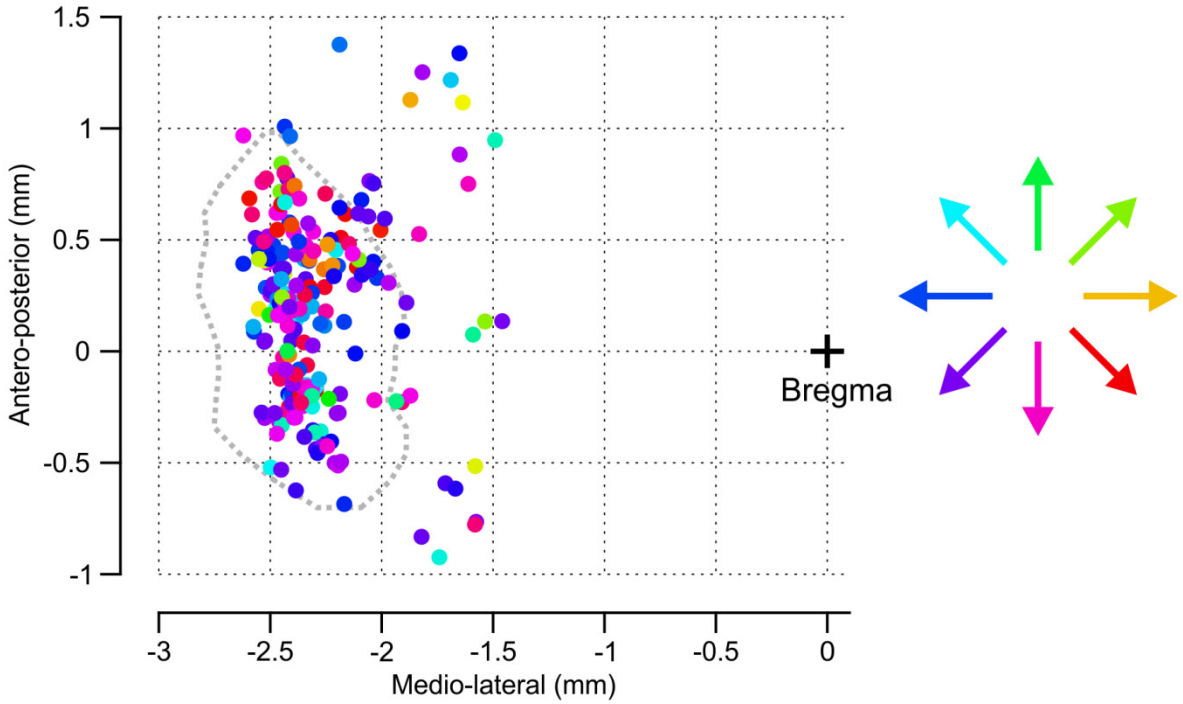

Supplementary Figure 3. Absence of directional topography in fS1. Antero-posterior and medio-lateral coordinates relative to bregma of directionally tuned proprioceptive neurons (N=225 neurons, 17 mice). The color code corresponds to the neuron's preferred direction. Gray dotted contour: limits of fS1 based on the mouse brain atlas (Paxinos, 2001).

Supplementary Movie 1. Passive forelimb displacement task. Example trial in the passive forelimb displacement task with a robotic manipulandum.

Supplementary Movie 2. 3D tracking of joint positions. 3D positions of 4 joints and the limb endpoint as well as their 2D projections were obtained for every manipulandum position in the tested planar workspace (red grid).

Supplementary Movie 3. Perceptual discrimination of proprioceptive stimuli. Example adduction and abduction trials in the two-alternative forced choice (2AFC) discrimination task.

References

Bale, M.R., and Petersen, R.S. (2009). Transformation in the neural code for whisker deflection direction along the lemniscal pathway. Journal of neurophysiology *102*, 2771-2780.

Bandet, M.V., Dong, B., and Winship, I.R. (2021). Distinct patterns of activity in individual cortical neurons and local networks in primary somatosensory cortex of mice evoked by square-wave mechanical limb stimulation. PLoS One *16*, e0236684.

Brecht, M. (2017). The Body Model Theory of Somatosensory Cortex. Neuron *94*, 985-992.

Campion, G., Qi, W., and Hayward, V. (2005). The Pantograph Mk-II: a haptic instrument. Paper presented at: 2005 IEEE/RSJ International Conference on Intelligent Robots and Systems.

Chapin, J.K., and Lin, C.S. (1984). Mapping the body representation in the SI cortex of anesthetized and awake rats. The Journal of comparative neurology *229*, 199-213.

Chapin, J.K., Sadeq, M., and Guise, J.L.U. (1987). Corticocortical connections within the primary somatosensory cortex of the rat. Journal of Comparative Neurology *263*, 326-346.

Cheney, P.D., and Preston, J.B. (1976). Classification and response characteristics of muscle spindle afferents in the primate. Journal of neurophysiology *39*, 1-8.

Chowdhury, R.H., Glaser, J.I., and Miller, L.E. (2020). Area 2 of primary somatosensory cortex encodes kinematics of the whole arm. Elife *9*.

Cooke, D.F., Padberg, J., Zahner, T., and Krubitzer, L. (2012). The functional organization and cortical connections of motor cortex in squirrels. Cerebral cortex (New York, NY : 1991) *22*, 1959-1978.

Costanzo, R.M., and Gardner, E.P. (1981). Multiple-joint neurons in somatosensory cortex of awake monkeys. Brain research *214*, 321-333.

Dadarlat, M.C., O'Doherty, J.E., and Sabes, P.N. (2015). A learning-based approach to artificial sensory feedback leads to optimal integration. Nature neuroscience *18*, 138-144.

Delhaye, B.P., Long, K.H., and Bensmaia, S.J. (2018). Neural Basis of Touch and Proprioception in Primate Cortex. Comprehensive Physiology *8*, 1575-1602.

Dimitriou, M., and Edin, B.B. (2008a). Discharges in Human Muscle Receptor Afferents during Block Grasping. The Journal of Neuroscience *28*, 12632.

Dimitriou, M., and Edin, B.B. (2008b). Discharges in human muscle spindle afferents during a key-pressing task. The Journal of physiology *586*, 5455-5470.

Edin, B.B., and Vallbo, A.B. (1990). Dynamic response of human muscle spindle afferents to stretch. Journal of neurophysiology *63*, 1297-1306.

Favorov, O.V., Pellicer-Morata, V., DeJongh Curry, A.L., Ramshur, J.T., Brna, A., Challener, T.D., and Waters, R.S. (2019). A newly identified nociresponsive region in the transitional zone (TZ) in rat sensorimotor cortex. Brain research *1717*, 228-234.

Fiser, A., Mahringer, D., Oyibo, H.K., Petersen, A.V., Leinweber, M., and Keller, G.B. (2016). Experience-dependent spatial expectations in mouse visual cortex. Nature neuroscience *19*, 1658-1664.

Friedrich, J., Zhou, P., and Paninski, L. (2017). Fast online deconvolution of calcium imaging data. PLOS Computational Biology *13*, e1005423.

Fuentes, C.T., and Bastian, A.J. (2010). Where is your arm? Variations in proprioception across space and tasks. Journal of neurophysiology *103*, 164-171.

Fyhn, M., Molden, S., Witter, M.P., Moser, E.I., and Moser, M.B. (2004). Spatial representation in the entorhinal cortex. Science (New York, NY) *305*, 1258-1264.

Georgopoulos, A.P., Kalaska, J.F., Caminiti, R., and Massey, J.T. (1982). On the relations between the direction of two-dimensional arm movements and cell discharge in primate motor cortex. The Journal of Neuroscience *2*, 1527.

Gilad, A., and Helmchen, F. (2020). Spatiotemporal refinement of signal flow through association cortex during learning. Nature communications *11*, 1744.

Giovannucci, A., Friedrich, J., Gunn, P., Kalfon, J., Brown, B.L., Koay, S.A., Taxidis, J., Najafi, F., Gauthier, J.L., Zhou, P.*, et al.* (2019). CaImAn an open source tool for scalable calcium imaging data analysis. eLife *8*, e38173.

González-Grandón, X., Falcón-Cortés, A., and Ramos-Fernández, G. (2021). Proprioception in Action: A Matter of Ecological and Social Interaction. Frontiers in Psychology *11*.

Goodman, J.M., Tabot, G.A., Lee, A.S., Suresh, A.K., Rajan, A.T., Hatsopoulos, N.G., and Bensmaia, S. (2019). Postural Representations of the Hand in the Primate Sensorimotor Cortex. Neuron *104*, 1000-1009.e1007.

Guo, Z.V., Li, N., Huber, D., Ophir, E., Gutnisky, D., Ting, J.T., Feng, G., and Svoboda, K. (2014). Flow of cortical activity underlying a tactile decision in mice. Neuron *81*, 179-194.

Keller, G.B., and Mrsic-Flogel, T.D. (2018). Predictive Processing: A Canonical Cortical Computation. Neuron *100*, 424-435.

Krubitzer, L., Huffman, K.J., Disbrow, E., and Recanzone, G. (2004). Organization of area 3a in macaque monkeys: contributions to the cortical phenotype. The Journal of comparative neurology *471*, 97-111.

Li, N., Chen, S., Guo, Z.V., Chen, H., Huo, Y., Inagaki, H.K., Chen, G., Davis, C., Hansel, D., Guo, C.*, et al.* (2019). Spatiotemporal constraints on optogenetic inactivation in cortical circuits. eLife *8*, e48622.

London, B.M., and Miller, L.E. (2013). Responses of somatosensory area 2 neurons to actively and passively generated limb movements. Journal of neurophysiology *109*, 1505-1513.

Long, X., and Zhang, S.-J. (2021). A novel somatosensory spatial navigation system outside the hippocampal formation. Cell Research *31*, 649-663.

Lucas, A., Tomlinson, T., Rohani, N., Chowdhury, R., Solla, S.A., Katsaggelos, A.K., and Miller, L.E. (2019). Neural Networks for Modeling Neural Spiking in S1 Cortex. Frontiers in Systems Neuroscience *13*.

Mahan, M., and Georgopoulos, A. (2013). Motor directional tuning across brain areas: directional resonance and the role of inhibition for directional accuracy. Frontiers in Neural Circuits *7*.

Mathewson, M.A., Chapman, M.A., Hentzen, E.R., Fridén, J., and Lieber, R.L. (2012). Anatomical, architectural, and biochemical diversity of the murine forelimb muscles. J Anat *221*, 443-451.

Morandell, K., and Huber, D. (2017). The role of forelimb motor cortex areas in goal directed action in mice. Scientific reports *7*, 15759.

Muñoz-Castañeda, R., Zingg, B., Matho, K.S., Chen, X., Wang, Q., Foster, N.N., Li, A., Narasimhan, A., Hirokawa, K.E., Huo, B.*, et al.* (2021). Cellular anatomy of the mouse primary motor cortex. Nature *598*, 159-166.

O'Connor, D.H., Krubitzer, L., and Bensmaia, S. (2021). Of mice and monkeys: Somatosensory processing in two prominent animal models. Progress in neurobiology *201*, 102008.

Paxinos, G. (2001). The mouse brain in stereotaxic coordinates / George Paxinos, Keith B.J. Franklin (San Diego, Calif. ; London: Academic).

Priebe, N.J., and Ferster, D. (2005). Direction selectivity of excitation and inhibition in simple cells of the cat primary visual cortex. Neuron *45*, 133-145.

Proske, U., and Gandevia, S.C. (2012). The proprioceptive senses: their roles in signaling body shape, body position and movement, and muscle force. Physiological reviews *92*, 1651-1697.

Prsa, M., Galiñanes, G.L., and Huber, D. (2017). Rapid Integration of Artificial Sensory Feedback during Operant Conditioning of Motor Cortex Neurons. Neuron *93*, 929-939 e926.

Prsa, M., Morandell, K., Cuenu, G., and Huber, D. (2019). Feature-selective encoding of substrate vibrations in the forelimb somatosensory cortex. Nature *567*, 384-388.

Prud'homme, M.J., and Kalaska, J.F. (1994). Proprioceptive activity in primate primary somatosensory cortex during active arm reaching movements. Journal of neurophysiology *72*, 2280-2301.

Sauer, J.-F., Folschweiller, S., and Bartos, M. (2022). Topographically organized representation of space and context in the medial prefrontal cortex. Proceedings of the National Academy of Sciences *119*, e2117300119.

Schütt, H.H., Harmeling, S., Macke, J.H., and Wichmann, F.A. (2016). Painfree and accurate Bayesian estimation of psychometric functions for (potentially) overdispersed data. Vision research *122*, 105-123.

Sigl-Glöckner, J., Maier, E., Takahashi, N., Sachdev, R., Larkum, M., and Brecht, M. (2019). Effects of Sexual Experience and Puberty on Mouse Genital Cortex revealed by Chronic Imaging. Current biology : CB *29*, 3588-3599 e3584.

Soechting, J.F. (1982). Does position sense at the elbow reflect a sense of elbow joint angle or one of limb orientation? Brain research *248*, 392-395.

Swanson, L.W., and Köhler, C. (1986). Anatomical evidence for direct projections from the entorhinal area to the entire cortical mantle in the rat. The Journal of neuroscience : the official journal of the Society for Neuroscience *6*, 3010-3023.

Tennant, K.A., Adkins, D.L., Donlan, N.A., Asay, A.L., Thomas, N., Kleim, J.A., and Jones, T.A. (2011). The organization of the forelimb representation of the C57BL/6 mouse motor cortex as defined by intracortical microstimulation and cytoarchitecture. Cerebral cortex (New York, NY : 1991) *21*, 865-876.

Thyrion, C., and Roll, J.-P. (2010). Predicting Any Arm Movement Feedback to Induce Three-Dimensional Illusory Movements in Humans. Journal of neurophysiology *104*, 949-959.

Tillery, S.I., Soechting, J.F., and Ebner, T.J. (1996). Somatosensory cortical activity in relation to arm posture: nonuniform spatial tuning. Journal of neurophysiology *76*, 2423-2438.

Town, S.M., Brimijoin, W.O., and Bizley, J.K. (2017). Egocentric and allocentric representations in auditory cortex. PLoS biology *15*, e2001878.

Tuthill, J.C., and Azim, E. (2018). Proprioception. Current Biology *28*, R194-R203.

Vigaru, B.C., Lambercy, O., Schubring-Giese, M., Hosp, J.A., Schneider, M., Osei-Atiemo, C., Luft, A., and Gassert, R. (2013). A robotic platform to assess, guide and perturb rat forelimb movements. IEEE transactions on neural systems and rehabilitation engineering : a publication of the IEEE Engineering in Medicine and Biology Society *21*, 796-805.

Wagner, M.J., Savall, J., Kim, T.H., Schnitzer, M.J., and Luo, L. (2020). Skilled reaching tasks for head-fixed mice using a robotic manipulandum. Nature protocols *15*, 1237-1254.

Wikenheiser, A.M., Gardner, M.P.H., Mueller, L.E., and Schoenbaum, G. (2021). Spatial Representations in Rat Orbitofrontal Cortex. The Journal of Neuroscience *41*, 6933.

Wilber, A.A., Clark, B.J., Forster, T.C., Tatsuno, M., and McNaughton, B.L. (2014). Interaction of egocentric and world-centered reference frames in the rat posterior parietal cortex. The Journal of neuroscience : the official journal of the Society for Neuroscience *34*, 5431-5446.

Xu, D., Dong, M., Chen, Y., Delgado, A.M., Hughes, N.C., Zhang, L., and O'Connor, D.H. (2022). Cortical processing of flexible and context-dependent sensorimotor sequences. Nature *603*, 464-469.

Yin, A., Tseng, P.H., Rajangam, S., Lebedev, M.A., and Nicolelis, M.A.L. (2018). Place Cell-Like Activity in the Primary Sensorimotor and Premotor Cortex During Monkey Whole-Body Navigation. Scientific reports *8*, 9184-9184.

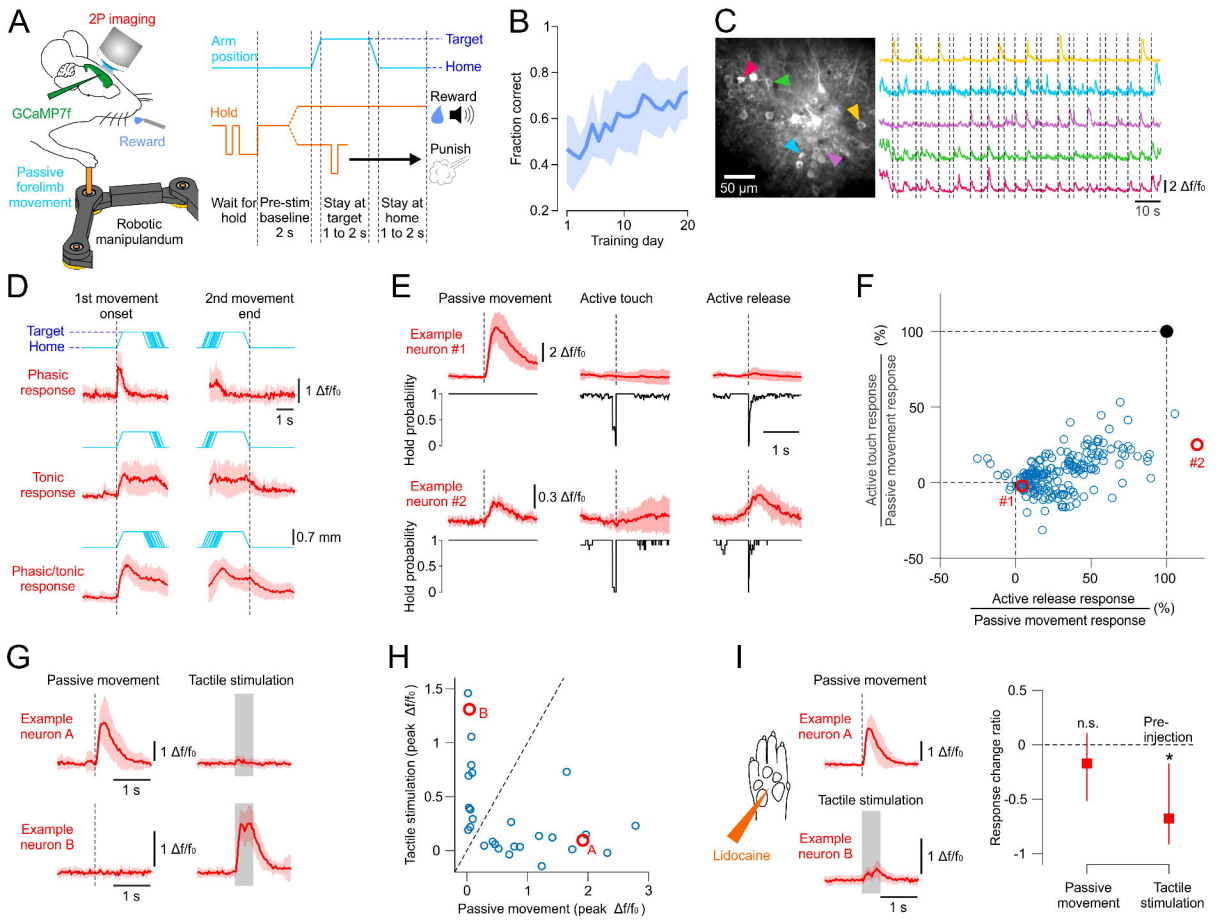
A
2P imaging
GCaMP7f
Reward
Passive forelimb movement
Robotic manipulandum
Arm position
Target
Home
Hold
Reward
Punish
Wait for hold
Pre-stim baseline 2 s
Stay at target 1 to 2 s
Stay at home 1 to 2 s
B
Fraction correct
Training day
C
50 µm
2 Δf/f0
10 s
D
1st movement onset
2nd movement end
Target
Home
Phasic response
Tonic response
Phasic/tonic response
1 Δf/f0
1 s
0.7 mm
E
Passive movement
Active touch
Active release
Example neuron #1
Example neuron #2
2 Δf/f0
0.3 Δf/f0
Hold probability
1 s
F
Active touch response / Passive movement response (%)
Active release response / Passive movement response (%)
#1
#2
G
Passive movement
Tactile stimulation
Example neuron A
Example neuron B
1 Δf/f0
1 s
H
Tactile stimulation (peak Δf/f0)
Passive movement (peak Δf/f0)
A
B
I
Passive movement
Tactile stimulation
Example neuron A
Example neuron B
Lidocaine
1 Δf/f0
1 s
Response change ratio
n.s.
Pre-injection
*
Passive movement
Tactile stimulation

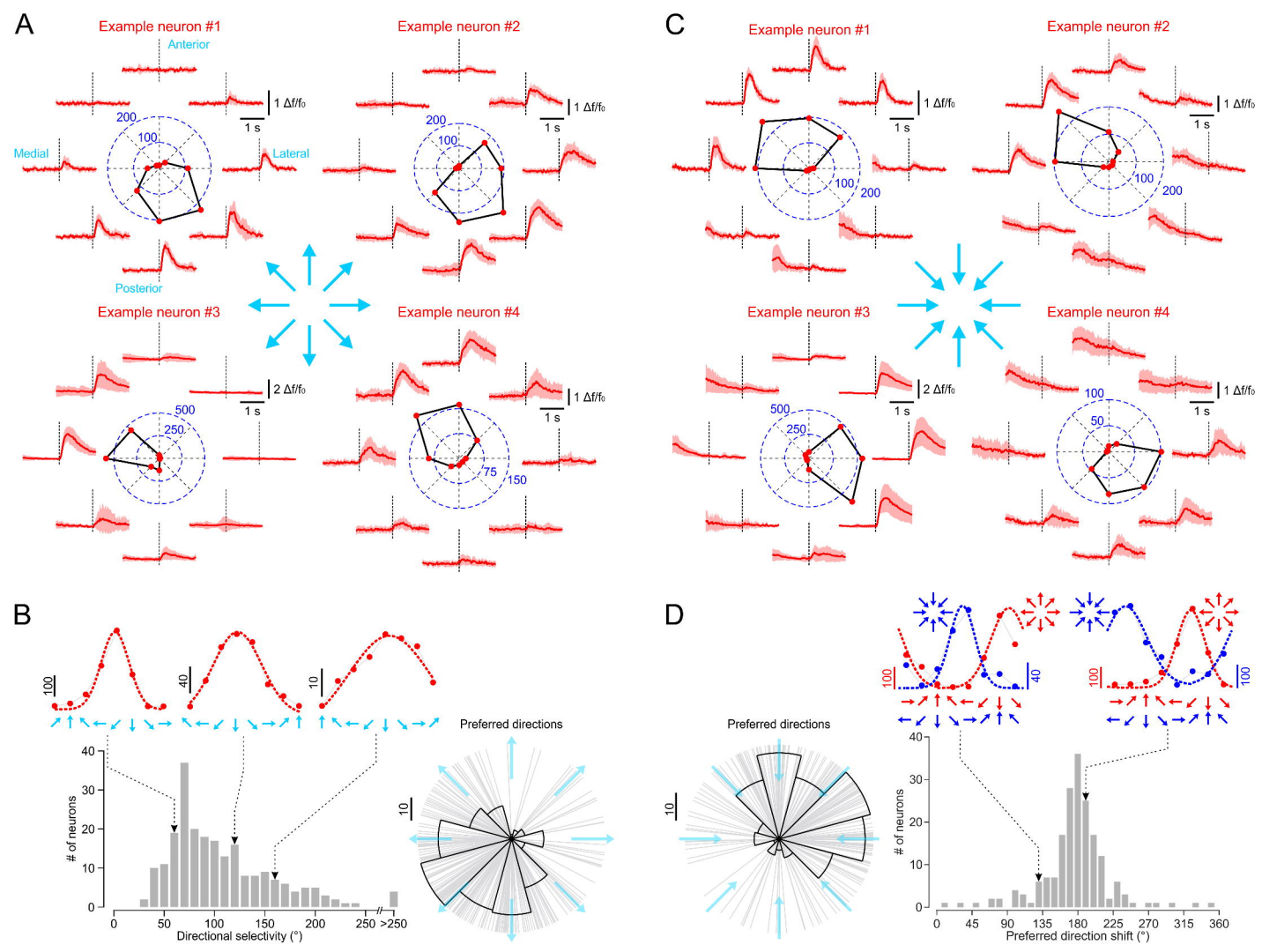
A
Example neuron #1
Anterior
Medial
Lateral
Posterior
1 Δf/f0
1 s
200
100
Example neuron #2
Example neuron #3
2 Δf/f0
500
250
Example neuron #4
75
150
C
Example neuron #1
Example neuron #2
Example neuron #3
Example neuron #4
50
B
100
40
10
Preferred directions
# of neurons
Directional selectivity (°)
0
50
100
150
200
250
>250
D
Preferred direction shift (°)
0
45
90
135
180
225
270
315
360

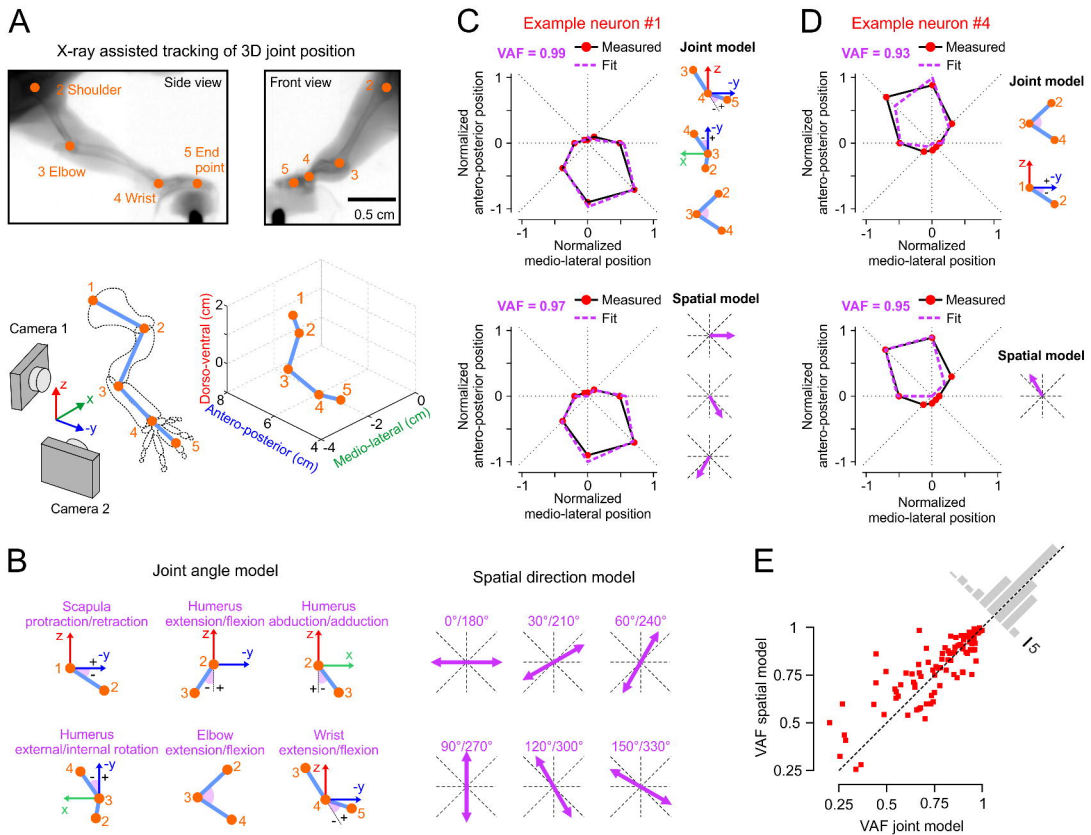
A
X-ray assisted tracking of 3D joint position
Side view
Front view
2 Shoulder
3 Elbow
4 Wrist
5 End point
0.5 cm
Camera 1
Camera 2
Dorso-ventral (cm)
Antero-posterior (cm)
Medio-lateral (cm)
C
Example neuron #1
VAF = 0.99
Measured
Fit
Joint model
Normalized antero-posterior position
Normalized medio-lateral position
VAF = 0.97
Spatial model
D
Example neuron #4
VAF = 0.93
VAF = 0.95
B
Joint angle model
Scapula protraction/retraction
Humerus extension/flexion
Humerus abduction/adduction
Humerus external/internal rotation
Elbow extension/flexion
Wrist extension/flexion
Spatial direction model
0°/180°
30°/210°
60°/240°
90°/270°
120°/300°
150°/330°
E
VAF spatial model
VAF joint model
15

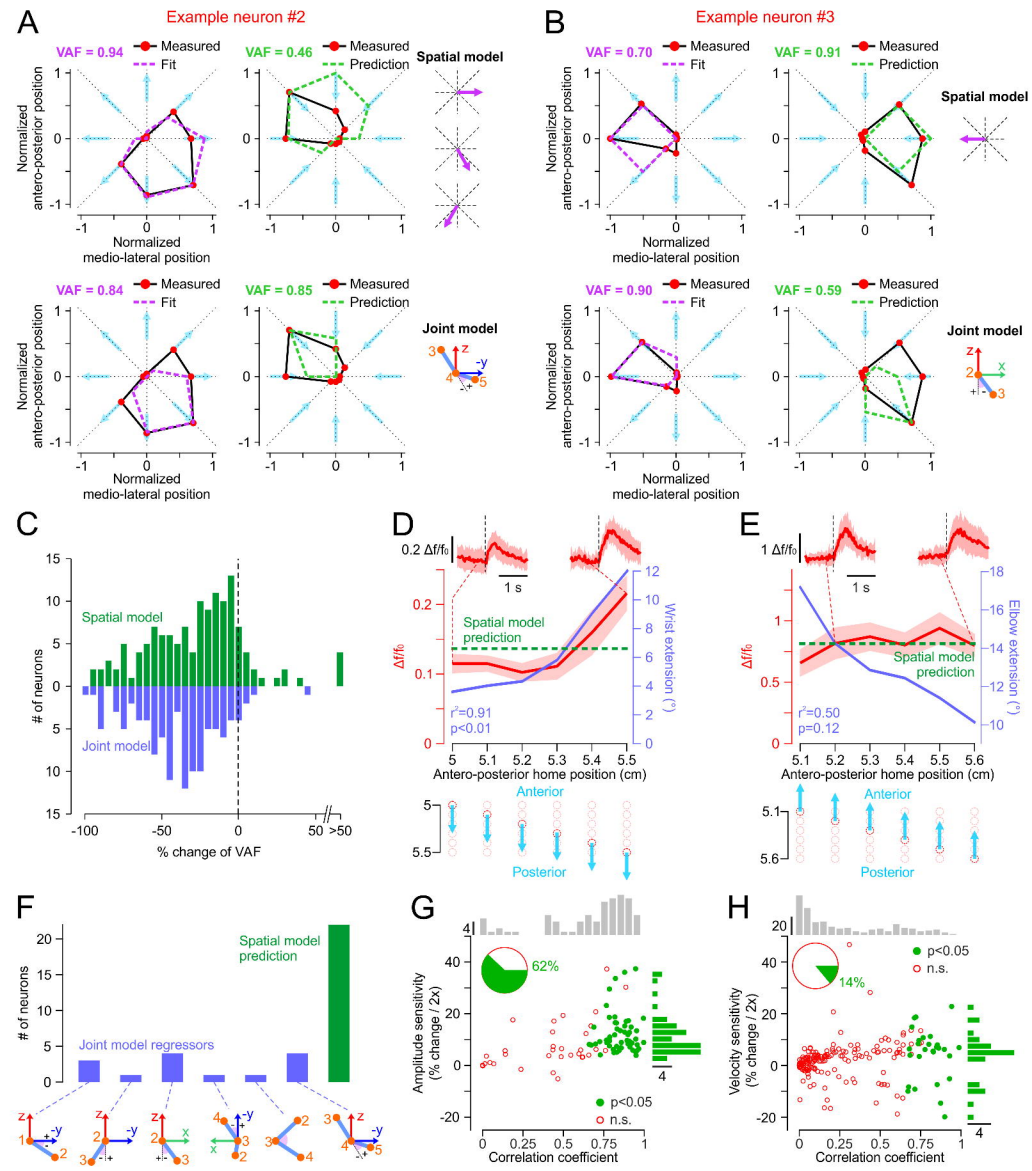
A
Example neuron #2
VAF = 0.94
Measured
Fit
VAF = 0.46
Measured
Prediction
Spatial model
Normalized antero-posterior position
Normalized medio-lateral position
VAF = 0.84
Measured
Fit
VAF = 0.85
Measured
Prediction
Joint model
B
Example neuron #3
VAF = 0.70
Measured
Fit
VAF = 0.91
Measured
Prediction
Spatial model
VAF = 0.90
Measured
Fit
VAF = 0.59
Measured
Prediction
Joint model
C
Spatial model
Joint model
# of neurons
% change of VAF
D
0.2 Δf/f0
1 s
Spatial model prediction
Δf/f0
Wrist extension (°)
r²=0.91
p<0.01
Antero-posterior home position (cm)
Anterior
Posterior
E
1 Δf/f0
1 s
Spatial model prediction
Δf/f0
Elbow extension (°)
r²=0.50
p=0.12
Antero-posterior home position (cm)
Anterior
Posterior
F
# of neurons
Spatial model prediction
Joint model regressors
G
62%
Amplitude sensitivity (% change / 2x)
p<0.05
n.s.
Correlation coefficient
H
14%
Velocity sensitivity (% change / 2x)
p<0.05
n.s.
Correlation coefficient

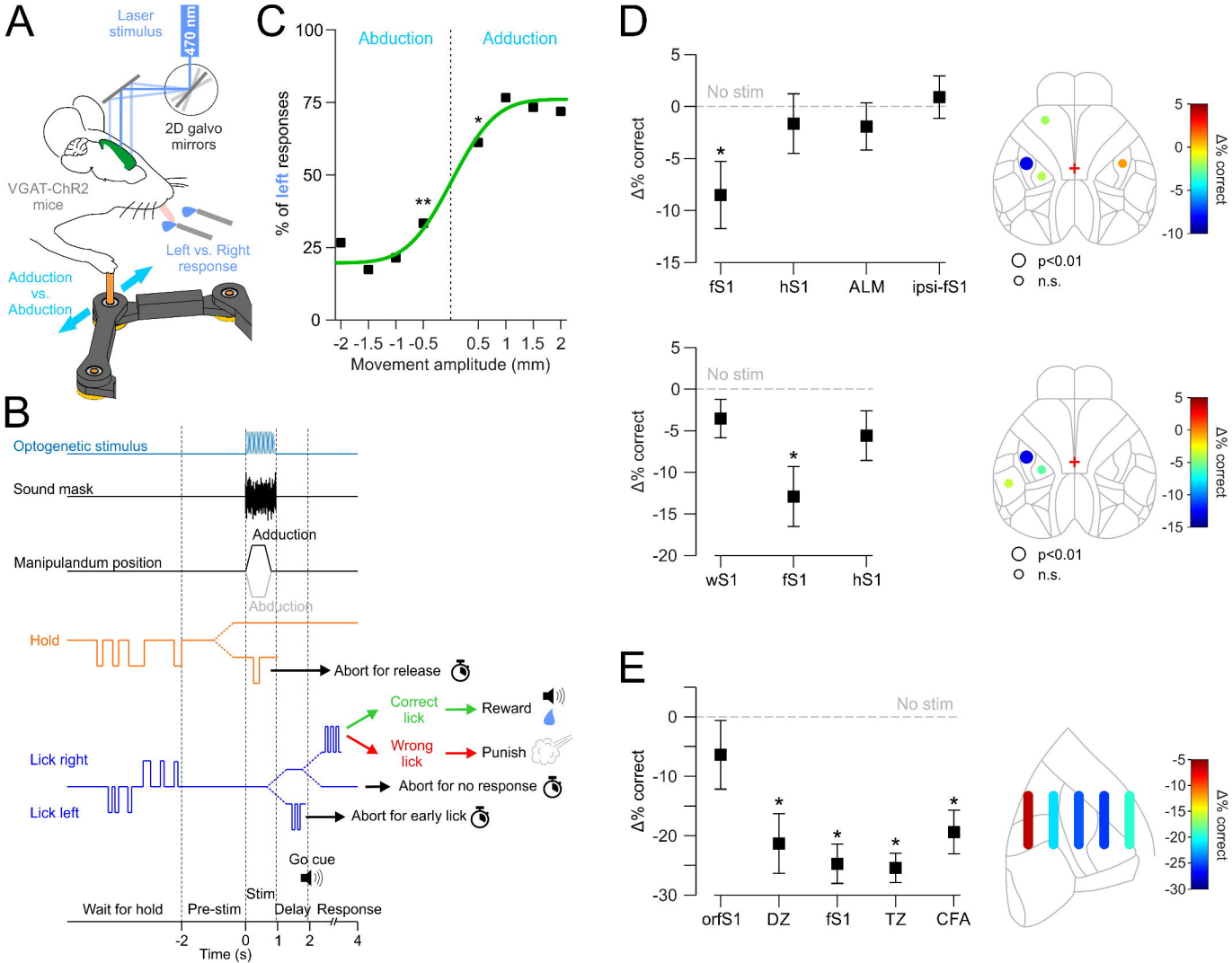
A
Laser stimulus
470 nm
2D galvo mirrors
VGAT-ChR2 mice
Left vs. Right response
Adduction vs. Abduction
C
Abduction
Adduction
% of left responses
Movement amplitude (mm)
B
Optogenetic stimulus
Sound mask
Adduction
Manipulandum position
Abduction
Hold
Abort for release
Correct lick
Reward
Wrong lick
Punish
Lick right
Abort for no response
Lick left
Abort for early lick
Go cue
Stim
Wait for hold
Pre-stim
Delay
Response
Time (s)
D
No stim
Δ% correct
fS1
hS1
ALM
ipsi-fS1
p<0.01
n.s.
wS1
E
orfS1
DZ
TZ
CFA

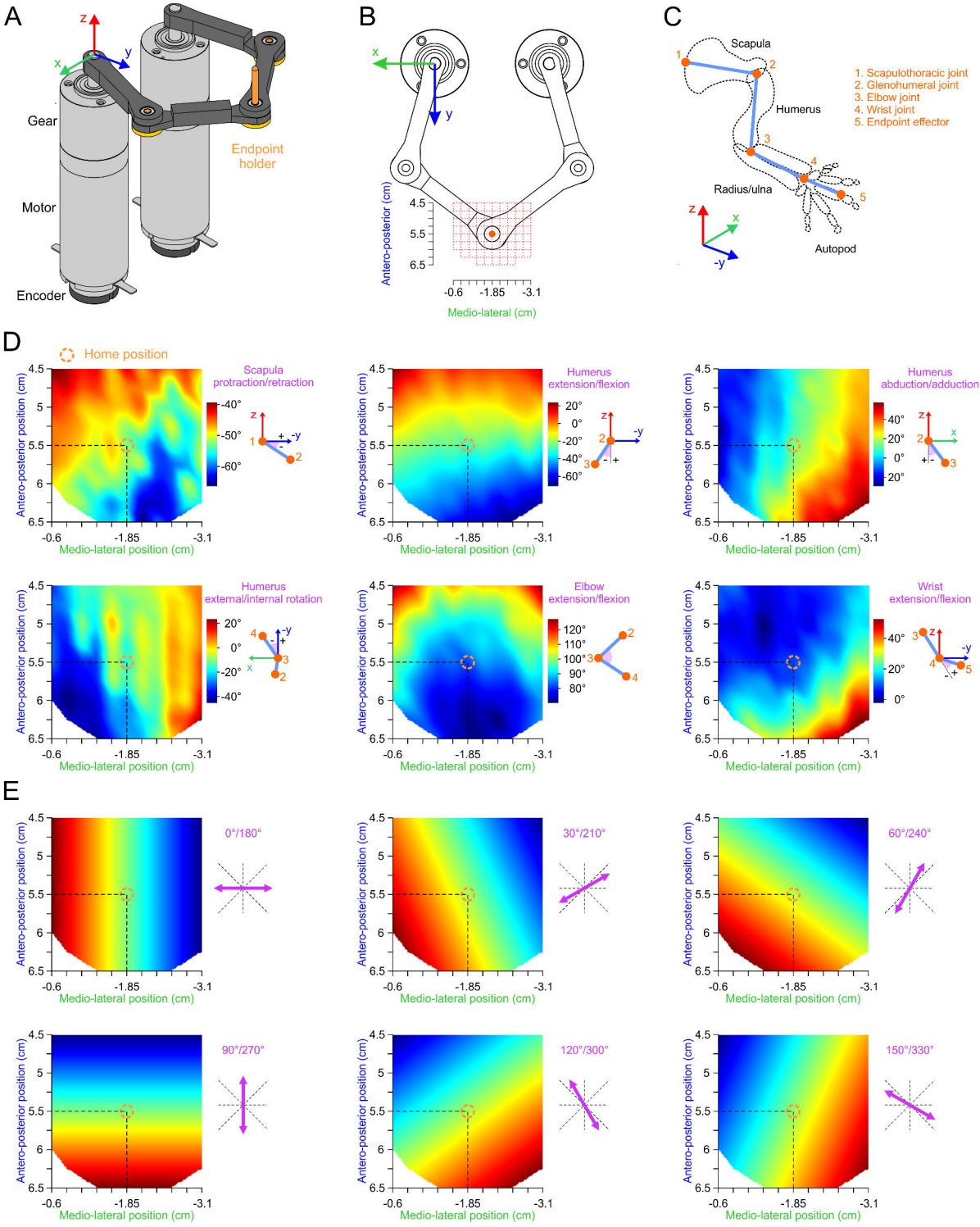
A
z
x
y
Gear
Endpoint holder
Motor
Encoder
B
x
y
Antero-posterior (cm)
4.5
5.5
6.5
-0.6
-1.85
-3.1
Medio-lateral (cm)
C
Scapula
Humerus
Radius/ulna
Autopod
1. Scapulothoracic joint
2. Glenohumeral joint
3. Elbow joint
4. Wrist joint
5. Endpoint effector
D
Home position
Scapula protraction/retraction
-40°
-50°
-60°
Humerus extension/flexion
20°
0°
-20°
-40°
-60°
Humerus abduction/adduction
40°
20°
0°
20°
Humerus external/internal rotation
20°
0°
-20°
-40°
Elbow extension/flexion
120°
110°
100°
90°
80°
Wrist extension/flexion
40°
20°
0°
Antero-posterior position (cm)
Medio-lateral position (cm)
E
0°/180°
30°/210°
60°/240°
90°/270°
120°/300°
150°/330°

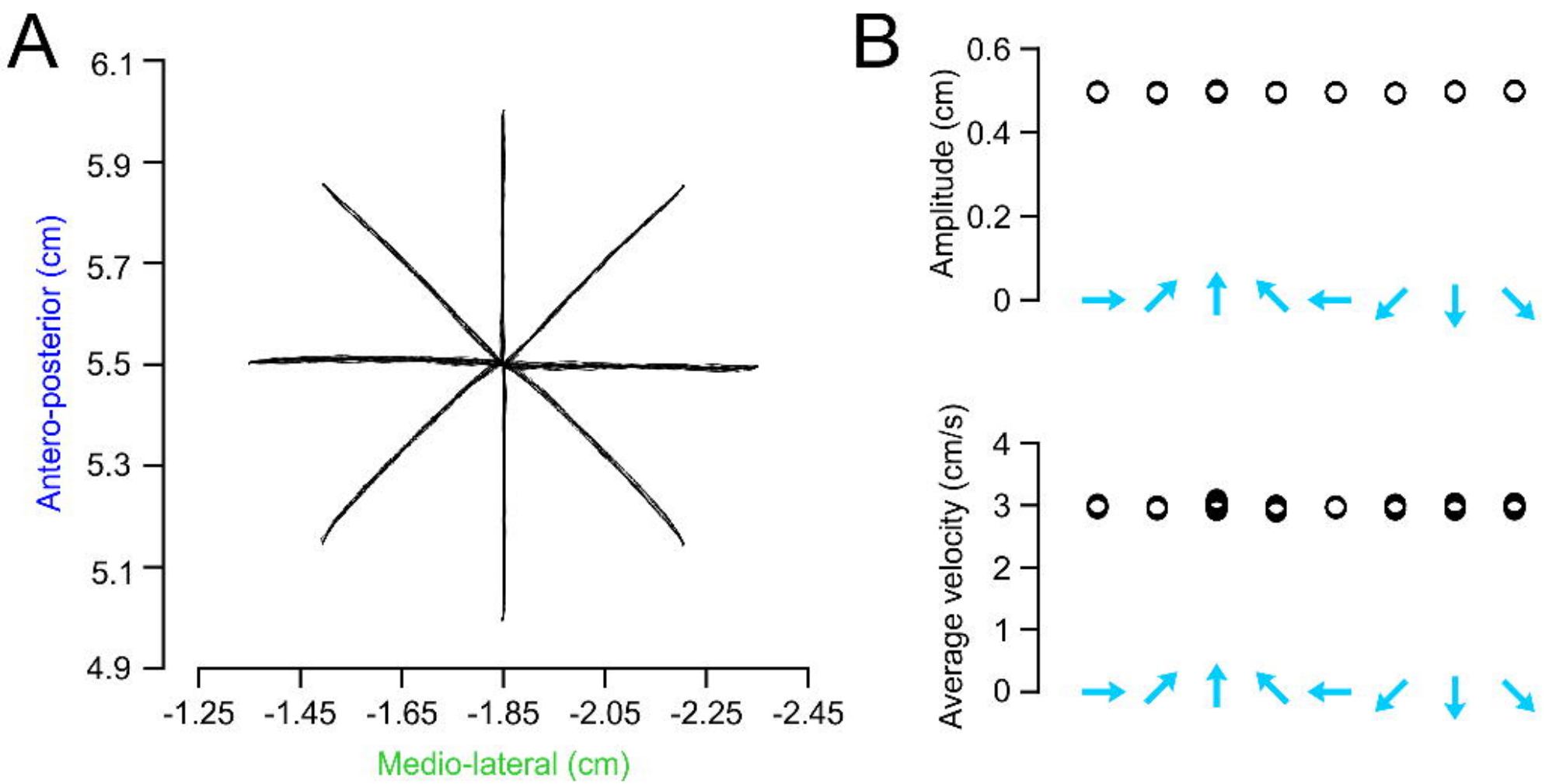
A
6.1
5.9
5.7
5.5
5.3
5.1
4.9
Antero-posterior (cm)
-1.25
-1.45
-1.65
-1.85
-2.05
-2.25
-2.45
Medio-lateral (cm)
B
0.6
0.4
0.2
0
Amplitude (cm)
4
3
2
1
0
Average velocity (cm/s)

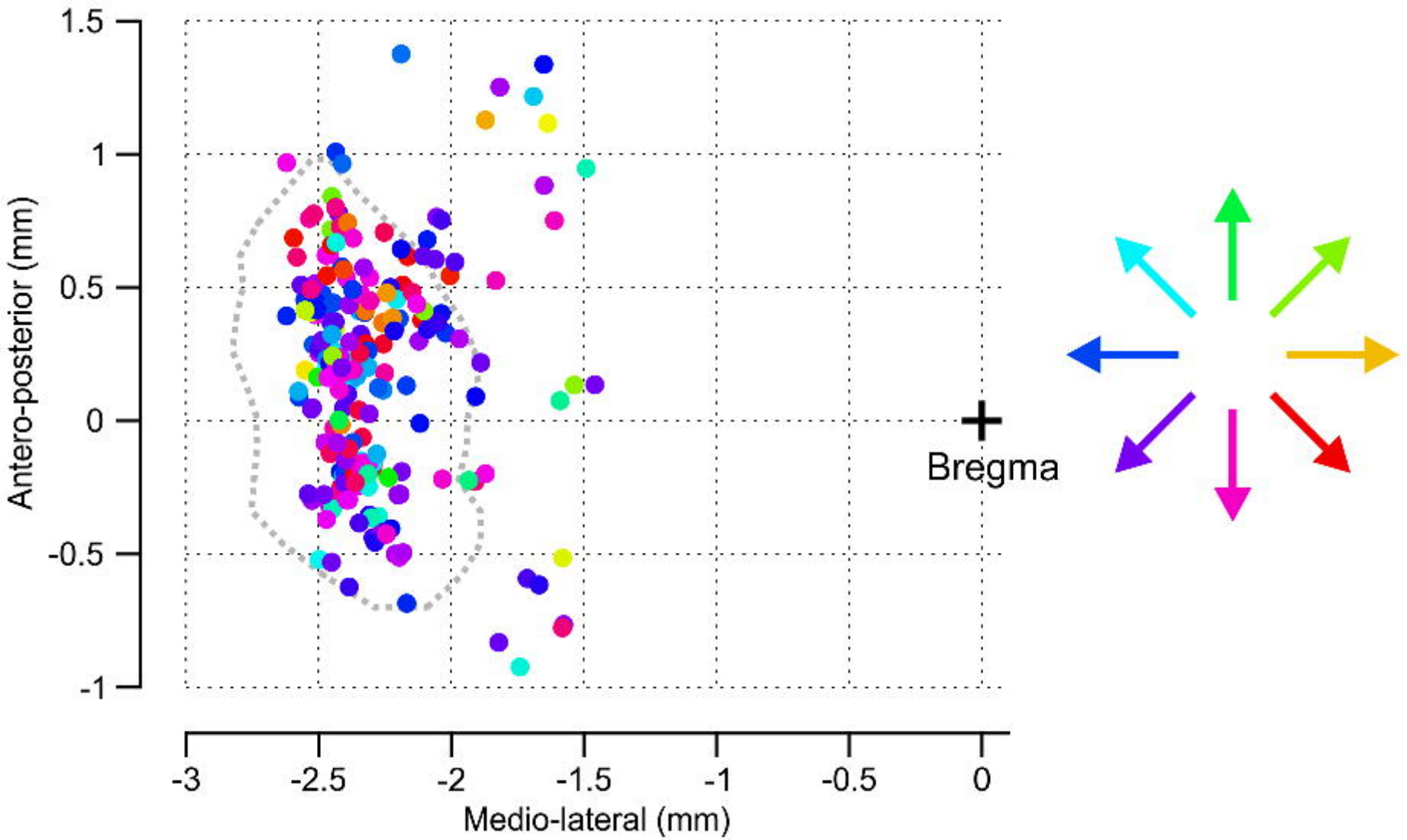
1.5
1
0.5
0
-0.5
-1
Antero-posterior (mm)
-3
-2.5
-2
-1.5
-1
-0.5
0
Medio-lateral (mm)
Bregma